Engineering 6 (2020) 992–1005

Contents lists available at ScienceDirect

Engineering

journal homepage: www.elsevier.com/locate/eng

Research
Energetic Materials and Interdisciplinary Science—Review

Novel X-Ray and Optical Diagnostics for Studying Energetic Materials: A Review

Yiyang Zhang [a], Sen Chen [a], Yang Cai [a], Lei Lu [b], Duan Fan [a], Jinchun Shi [a,*], Junyu Huang [a,*], Sheng-Nian Luo [b]

[a] The Peac Institute of Multiscale Sciences, Chengdu 610031, China
[b] School of Materials Science and Engineering, Southwest Jiaotong University, Chengdu 610031, China

ARTICLE INFO

Article history:
Received 6 April 2020
Revised 25 May 2020
Accepted 3 June 2020
Available online 11 August 2020

Keywords:
Energetic materials
X-ray
Terahertz and optical diagnostics
Multiscale measurements

ABSTRACT

Thermomechanical, physical, and chemical processes in energetic materials (EMs) during manufacturing and processing or under external stimuli such as shock compression, involve multiple temporal and spatial scales. Discovering novel phenomena, acquiring new data, and understanding underlying mechanisms all require temporally and spatially resolved diagnostics. Here, we present a brief review of novel diagnostics that are either emerging or have existed but rarely been applied to EMs, including two-dimensional (2D) and three-dimensional (3D) X-ray imaging, X-ray diffraction, coherent X-ray diffraction imaging, small angle X-ray scattering, terahertz and optical absorption/emission spectroscopy, and one-dimensional (1D) and 2D laser-based velocity/displacement interferometry. Typical spatial scales involved are lattice (nanometer and micrometer) and typical temporal scales (femtosecond, picosecond, nanosecond, microsecond, and millisecond). The targeted scientific questions and engineering problems include defects, strengths, deformations, hot spots, phase changes, reactions, and shock sensitivities. Basic principles of measurement and data analysis, and illustrative examples of these are presented. Advanced measurements and experimental complexities also necessitate further development in corresponding data analysis and interpretation methodologies, and multiscale modeling.

1. Introduction

Energetic materials (EMs) store large quantities of chemical energy, which can be released rapidly upon thermal or mechanical stimuli [1–4]. According to the amount of stored chemical energy and release rate, EMs are generally classified into explosives (primary or secondary explosives), propellants, and pyrotechnics [3,5]. Sustained interest in EMs has been driven by their wide civil and military applications as well as basic science [6]. A thorough understanding of mechanical, physical, and chemical processes in EMs is required not only to predict and control their performance, but also to address increasing environmental and safety concerns of EMs [1,7].

Thermomechanical, physical, and chemical processes in EMs during manufacturing and processing or under external stimuli such as shock compression, involve multiple temporal and spatial scales [6,8]. Microstructures (lattice defects, voids, cracks, interfaces, etc.) created during manufacturing and processing, ranging from sub-nanometers to millimeters [9,10], can impact their responses to external stimuli, and their subsequent chemical kinetics and overall performance [11,12]. Under thermal or mechanical stimuli, such microstructures may lead to strain, stress, or heating localizations, resulting in local chemical reactions ("hot spots") [13–16]. Upon external stimulation, mechanical and physical (e.g., plastic deformation [17,18], phase transition [19,20], and hot spot formation) and chemical (e.g., chemical kinetics [12,21] and carbon condensate formation [22,23]) processes in EMs span temporal scales from femtoseconds to microseconds, and spatial scales from single molecules and lattices to micrometers or larger. For example, shock-induced chemical initiation usually occurs at the molecular level and sub-picosecond scale [15,24–28]. Up to the mesoscale, the propagating shock wave interacts with the complex microstructure of an EM, yielding phase transitions and hot spots; the shock-to-detonation transition (SDT) [29] is manifested at the macroscale. The temporal scales in manufacturing and processing and external stimulation involve 100 fs in laser ablation [30,31], 100 ns in plate impact loading [32–34], 100 μs in split Hopkinson pressure bar (SHPB) loading [35,36], 10 ms in combustion shock tube [37,38], and 100 s in manufacturing. Given the

* Corresponding authors.
E-mail addresses: jcshi@pims.ac.cn (J. Shi), jyhuang@pims.ac.cn (J. Huang).

https://doi.org/10.1016/j.eng.2020.06.019

multiple temporal and spatial scales inherent in EMs at various stages of their life cycles, reliable engineering simulations must resort to physics-based predictive models that incorporate multiscale structures and physical and chemical dynamics [6,7,39], calling for temporally and spatially resolved measurements.

While static [9,40–42] or macroscale [18,34] characterizations of EMs have been routine, resolving structure and physical and chemical dynamics at the micro- and mesoscales and appropriate temporal resolutions have been a diagnostics challenge. Since the physical and chemical events in EMs upon external stimuli occur in extreme conditions [6,18,33], the diagnostics should be nondestructive and penetrating, with high spatial and temporal resolutions. Conventional techniques, such as optical microscopy with matching reflective index [43], confocal scanning laser microscopy [44], polarized light microscopy [33], and scanning electron microscopy [45], can only provide surface measurements, and should be complemented with diagnostics having see-through capability and proper temporal resolutions, or providing extra information. The remarkable progress in X-ray sources, terahertz (THz) sources, detectors, and spectroscopy and imaging systems [46,47] offer opportunities to address the diagnostics challenges for EMs. For example, advanced synchrotron X-ray sources [46,48] and X-ray free electron lasers (XFELs) [49,50] provide femtosecond- and picosecond-scale pulse durations, and unprecedentedly high spatial and temporal resolutions to resolve structure and physical and chemical dynamics in EMs.

Here, we present a brief review on novel X-ray and optical diagnostics for EMs that are either emerging or already exist but are rarely applied to EMs. These diagnostics are targeted for such scientific questions and engineering problems as defects, strengths [51], deformations [18], hot spots, phase changes, reactions, and shock sensitivities [52,53]. This review emphasizes their capabilities of temporally and/or spatially resolved measurements. In addition, basic principles of measurement and data analysis, and illustrative examples for these are presented. In Section 2, we present two-dimensional (2D) and three-dimensional (3D) X-ray imaging techniques including X-ray phase contrast imaging (PCI), X-ray computed tomography (CT), X-ray diffraction (XRD), coherent diffraction imaging (CDI), and small angle X-ray scattering (SAXS). Section 3 addresses THz and optical absorption and emission spectroscopy including THz absorption spectroscopy, pyrometry and laser-induced breakdown spectroscopy (LIBS), and ultrafast imaging interferometry, which includes one-dimensional (1D) and 2D velocity interferometer system for any reflector (VISAR) and transient imaging displacement interferometry (TIDI). Section 4 presents a summary of this review.

2. X-ray diagnostics

Advanced synchrotron and XFEL X-ray sources with high brilliance, high coherence, high repetition rate, and short pulse duration allow for *in situ*, real time, multiscale measurements on a wide range of materials and processes [49,50,54,55]. Common X-ray diagnostics are imaging in real space, diffraction and scattering in reciprocal space, and spectroscopy. X-ray spectroscopy is beyond the scope of this review and will not be discussed.

Different X-ray diagnostics involve different length scales and thus, different spatial resolutions. Fig. 1(a) illustrates three types of X-ray diagnostics: imaging (including PCI and CT), scattering (including SAXS), and XRD, with a typical length scale of micrometer and sub-micrometer, 1–100 nm, and lattice spacing (Å), respectively [46,56]. CDI is carried out in the Fourier space via phase retrieval and can achieve a spatial resolution of sub-nanometer scale. Such a rich suite of X-ray diagnostics renders structural characterization of EMs at multiple spatial scales feasible.

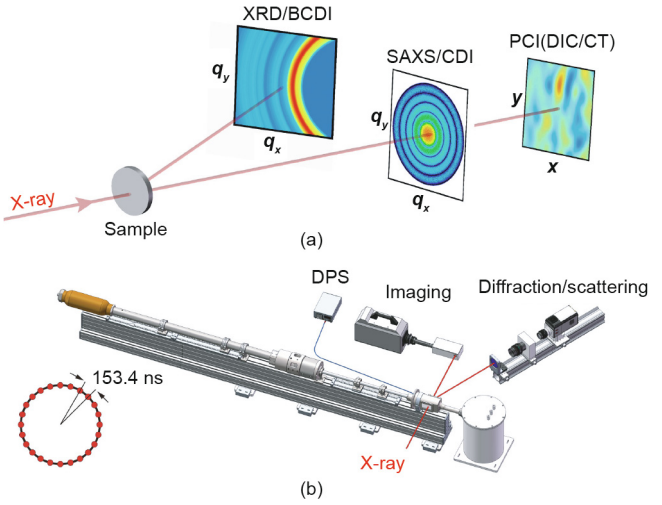

Fig. 1. *In situ* multiscale measurements with X-rays. (a) Schematic diagrams of XRD, SAXS/CDI, and PCI/CT techniques. Typical data of XRD, SAXS and digital image correlation (DIC) are shown. Here, $\boldsymbol{q_x}$ and $\boldsymbol{q_y}$ are basic vectors of reciprocal space, $\boldsymbol{x}$ and $\boldsymbol{y}$ are basic vectors of real space. (b) Experimental setup for gas-gun loading along with X-ray imaging and diffraction/scattering diagnostics shown in (a), and an optical interferometry system (Doppler pin system (DPS)). Loading can be delivered with materials testing systems (MTSs), SHPBs, lasers, magnetic-driven devices, shock tubes, and so on. Inset: time-structure of a typical synchrotron filling mode. BCDI: Bragg CDI.

For single-bunch synchrotron X-ray measurements, loading devices, X-ray shutters, X-ray pulse train, and detectors are timed against a radio frequency signal from the synchrotron, which serves as the master clock of synchronization among these four key components [46]. The temporal characteristics, i.e., pulse width and pulse separation of the X-ray pulse train, are dictated by the time structure of electron bunch filling. Fig. 1(b) inset shows an example of the standard filling pattern at the Advanced Photon Source: Pulse width is ~80 ps, and pulse separation is 153.4 ns. Correspondingly, the highest temporal resolution for X-ray measurements is limited by pulse width (~100 ps), and the framing rate, by pulse separation. For comparison, the highest temporal resolution in XFEL experiments is 10–100 fs; the shortest pulse separation is approximately 10 ms for linac coherent light source (LCLS), 1 μs for LCLS-II, and 220 ns for European XFEL. For microsecond-level resolution, the time structure of a synchrotron filling mode becomes irrelevant and the X-rays can be treated as a continuous wave, while temporal resolution is achieved with electronic shutters of detectors. Considering different temporal resolutions, physical and chemical processes in EMs can be investigated at multiple temporal scales, in addition to multiple length scales.

EMs can be subjected to different stimuli or loading, such as lasers, gas-guns, SHPBs, materials testing systems (MTSs), and shock tubes, with different loading rates, event durations, and stress and temperature conditions. The setup for synchrotron-based, *in situ*, real time, multiscale X-ray measurements [57], implemented with gas-gun loading, is shown in Fig. 1(b) as an example [56]. The projectile launched by a gas-gun impacts an EM target, inducing physicochemical changes, which are probed with X-ray imaging and diffraction, as well as an optical velocimeter. Since the event duration is of 100–1000 ns for gas-gun loading, single-bunch X-ray measurements are required.

2.1. X-ray PCI and digital image correlation

Propagation-based PCI extracts phase information as well as ensures the attenuation of an X-ray beam passing through a material [58,59]. A heterogeneous phase object induces spatial

variations in the phase of X-rays, $\phi(x, y)$, and local curvature in the transmitted wave front. The intensity change, $I(x, y)$, during propagation and interference of such wave fronts is proportional to the Laplacian of this phase distribution, $\nabla^2\phi(x, y)$, yielding edge enhancement [58].

$$I(x, y) \propto \nabla^2\phi(x, y) \quad (1)$$

Therefore, PCI is particularly suitable for high-resolution imaging of low-density materials like EMs. Currently, advanced X-ray PCI based on synchrotron radiation and XFELs allows for *in situ*, real-time imaging of internal deformation, damage, and reaction dynamics under dynamic loading, at 100 ps [46,56] and 10–100 fs [49,50] temporal resolutions, respectively.

Polymer bonded explosives (PBXs) are the most widely used insensitive high explosives [33,60]. Defects within crystals at the crystal-binder interface in the partially-dissolved crystal-binder region or within the binder itself may all contribute to hot spot nucleation [13,14] and initiate deflagration or detonation in abnormal conditions. High-speed synchrotron X-ray PCI has been utilized to characterize deformation and damage of PBXs under dynamic loading with ultrasound [35], SHPB [35,61], and gas gun [62,63]. The temporal and spatial resolutions can reach ~1 μs and 1–10 μm, respectively [46,48]. Fig. 2(a) displays the PCI images of an octahydro-1,3,5,7-tetranitro-1,3,5,7-tetrazocin (HMX)-based PBX sample with sparsely distributed crystal particles [35] under SHPB loading. The crystal particles can be clearly distinguished from the polymer matrix (which has a similar density) due to edge enhancement. The crystal-matrix delamination (at 95 μs) and particle breakage (at 240 μs) are manifested in the high-resolution PCI images.

Strain mapping across an EM sample, which highlights strain localizations and mechanical energy deposition, is crucial for understanding hot spot formation. X-ray projections of microstructures (e.g., crystal particles in PBX) can provide natural speckles for correlation analysis to track displacement/strain fields [64–66]. The calculation principle and procedure for X-ray digital image correlation (DIC) is similar to those for conventional optical DIC [67]. However, X-ray DIC provides smaller (50 μm or less) speckles and higher spatial resolution (10 μm or better) [68] due to PCI. The deformation dynamics can be resolved for local areas, e.g., particle–matrix interfaces in PBX. X-ray DIC is more advantageous when internal features (e.g., explosive crystal particles) are used to produce speckles through PCI [57,69]. Internal deformation can be studied on a length scale beyond optical DIC. Optical DIC is limited to low temperatures and may fail at or close to the detonation limit. On the other hand, X-ray DIC provides a flexible method for measuring both surface and internal deformation fields depending on how speckles are prepared, and opens new horizons for "2.5D" strain measurements. In addition, X-ray DIC can be combined with XRD to provide lattice-scale deformation mechanisms [48,57], as detailed in Section 2.4.

Fig. 2(b) presents the first study on X-ray DIC for strain mapping around a preset internal void in an aluminum plate under dynamic tension [64]. Lagrangian tensile (E_{11}) and shear (E_{12}) strain concentrations are observed to nucleate and grow around the void with increasing loading. The displacement and strain errors are below 0.01 pixels and 0.01%, respectively.

2.2. In situ and dynamic CT and mesoscale finite element modeling

Laboratory- or synchrotron-based CT serves as a unique tool for nondestructive, 3D characterization of microstructures of a variety of materials [70–72] including EMs [10,43,73,74]. With the rapid development of X-ray sources, *in situ* CT is gaining popularity in resolving deformation and failure of explosives or simulants under

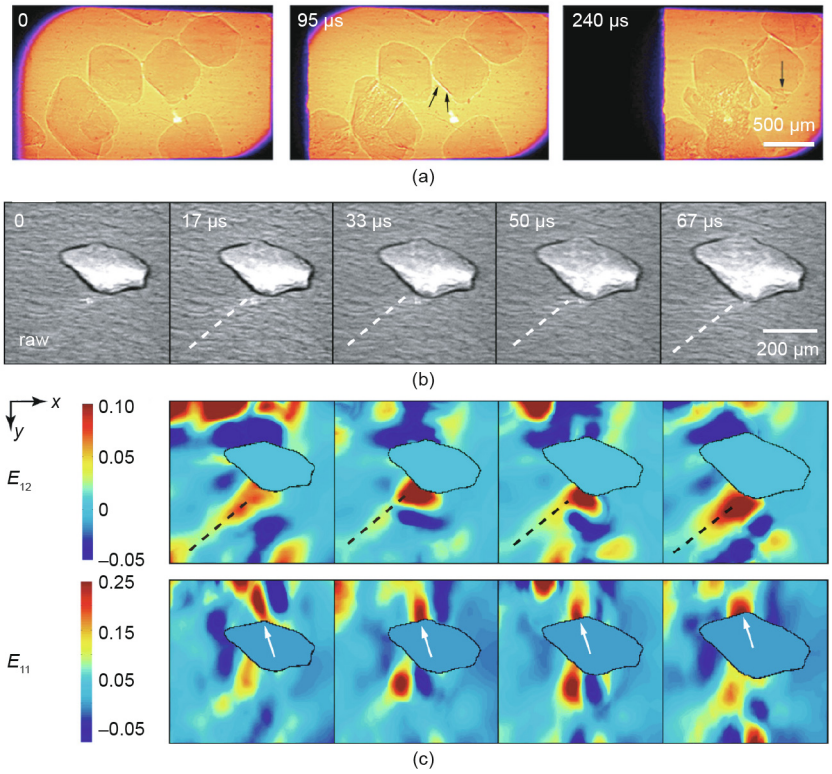

Fig. 2. (a) X-ray PCI image sequence of PBX under SHPB compression; (b) X-ray PCI image sequence of void growth in an aluminum plate under dynamic tension; (c) corresponding Lagrangian shear strain (E_{12}) and tensile strain (E_{11}) fields. (a) Reproduced from Ref. [35] with the permission of AIP Publishing, ©2016; (c) reproduced from Ref. [64] with the permission of AIP Publishing, ©2014.

mechanical loading (e.g., handling, transport, or green compaction) [75–78]. Various loading cells including miniature MTS were designed for *in situ* CT scanning [71,72]. Although laboratory CT can be used for *in situ* testing, synchrotron CT usually provides a much better combination of penetration and temporal and spatial resolutions [72]. Fig. 3(a) presents an example of CT characterization on a columnar granular packing under compression [70]. Particle rotation and breakage are clearly revealed in the 3D images, consistent with stress drops in the force displacement curve. 3D morphology of particles, intra-granular pores, and crack networks can be quantified via topological analysis including gyration tensor and fractal [70,79].

3D displacement/strain fields can be deduced from volume image sequences via digital volume correlation (DVC) [72,73,75]. For PBX samples, crystal particles serve as natural speckles for DVC. Various incremental DVC algorithms were developed for 3D deformation mapping [80]. 3D correlation criteria were proposed to establish the correspondence between reference and current frames, similar to DIC. Iterative correlation was usually used to achieve high accuracy. Fig. 3(c) [73] presents 3D microstructures from CT characterization and the corresponding DVC analyses for polymer-bonded sugar (PBS), an explosive simulant. Evolution of the axial displacement field in the PBS sample is well correlated to its heterogeneous microstructure, as well as debonding and particle breakage.

With synchrotron sources, the temporal resolution of CT can be increased to ~5 ms (208 tomograms per second) [81]. Such a dynamic CT has been applied to dynamic processes including foaming [81,82], sintering [83], and cracking [84,85]. Fig. 3(b) presents two representative 3D images of a bubble structure captured at 1 Hz. The velocity field of bubbles is quantified via particle imaging velocimetry (PIV) [86]. Such information is useful for understanding packing dynamics, for instance, during compaction of explosive crystals. Although the sub-second temporal resolution is insufficient to resolve highly transient impact or shock events, dynamic CT can capture the deformation dynamics of PBXs at low loading rates or map void production and fluid flow in PBXs during manufacturing and processing, or under thermal decomposition [87]. Recently, a high-speed CT system was demonstrated based on flash X-ray radiography with multiple sources and detectors at a sub-microsecond temporal resolution and a sub-millimeter spatial resolution [88], while the number and quality of tomograms remain to be improved via integrating more X-ray sources and detectors. Such techniques are promising for studying the shock detonation of EMs.

Moreover, 3D microstructures of PBXs obtained from dynamic CT can be used as inputs to and for comparison with finite element modeling (FEM) [67,89]. Details on the simulation procedures, material models, and parameters [89–91] are beyond the scope of this review. Fig. 3(d) shows that mesoscale FEM reproduces well the crystal-binder delamination and intergranular cracking [67]. However, 2D meshes with a limited number of crystal particles were employed in previous studies for simplicity [67,89]. The appropriate size for a 3D representative volume element at which macroscale behaviors can be adequately described remains to be elucidated [67,76]. With higher-resolution images and advanced image processing, mesoscale FEM with realistic, complex 3D configurations can be exceedingly useful for studying quantitatively the structure–property relations of PBXs, especially under high-rate, thermal-mechanical loading [20,90]. Meanwhile, phase transition and chemical reaction dynamics can be integrated into mesoscale FEM via user subroutine programs, e.g. UMAT/VUMAT [92].

2.3. XRD, CDI, and SAXS

2.3.1. XRD

XRD is essentially a manifestation of electron density distribution of atoms in an ordered/disordered lattice via scattered X-rays. Moreover, it is an indispensable tool for nondestructive determination of crystal structure, phase component, phase change and pathway, grain size, texture, deformation (including strain tensor), and indirectly residual stress and strength. XRD can be conducted on polycrystalline and single-crystal solids, as well as on liquids.

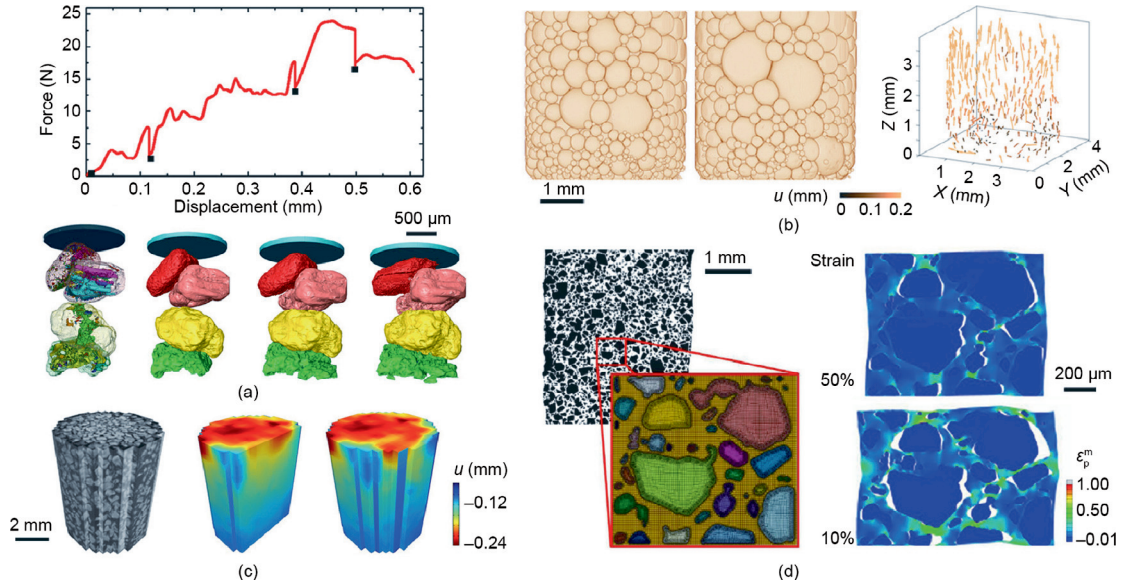

Fig. 3. (a) Force–displacement curve and 3D tomograms from *in situ* testing of a granular packing under compression with a miniature MTS at the displacements marked on the curve. (b) Dynamic CT characterizations of a foaming process at 1 Hz, displaying two tomograms (left) and displacement field u (right) obtained from PIV. (c) 3D axial displacement fields of a granular packing under quasi-static compression. (d) 2D FEM model based on a tomogram of a PBX sample (left) and simulated 2D maximum principal strain fields ε_p^m (right) at two volumetric strains. (a) Reproduced from Ref. [70] with the permission of Elsevier, ©2020; (b) and (c) reproduced from Ref. [73] with the permission of Elsevier, ©2012; (d) reproduced from Ref. [75] with the permission of MDPI, ©2017.

For instance, to elucidate the polymorphic structure of 1,3,5-trinitrohexahydro-1,3,5-triazine (RDX), a widely used explosive first synthesized in 1899 [93], has been investigated under ambient and high pressures regarding its polymorphism with combined single-crystal and powder diffraction. At ambient conditions, RDX exists as stable α-RDX and metastable β-RDX. Their crystal structures were obtained largely with single-crystal XRD [94–98]. RDX has a complex phase diagram, as determined with the diamond anvil cell (DAC) technique [19,40,99] and is rich in polymorphs, including γ-, δ-, ε-phases and the recently discovered ξ- and η-RDX [100].

Static-compression diffraction experiments on RDX were primarily conducted with DAC [40,101,102]. For shock compression, both *ex situ* and *in situ* XRD measurements were conducted on RDX [103,104], but no data have been published for the latter till date. Despite that, though dynamic XRD with a synchrotron or XFEL source has been well-established for shock compression [46,56,105,106], its applications to EMs are just emerging.

To illustrate the feasibility of applying transient X-ray diffraction (TXD) to investigating EMs under shock compression, we perform XRD simulations on single-crystal (Fig. 4) [102,107] and polycrystalline RDX (Fig. 5), regarding its phase change, equation of state, and strength upon simulated plate impact loading. In the simulations, diffraction intensity, I, of a simulated structure at scattering vector $\boldsymbol{q}$ is the product of structure factor $F(\boldsymbol{q})$ with its complex conjugate, $F*(\boldsymbol{q})$ [108,109], i.e.,

$$I(\boldsymbol{q}) = F*(\boldsymbol{q})F(\boldsymbol{q}) \tag{2}$$

with

$$F(\boldsymbol{q}) = \sum_{j=1}^{N} f_j \exp(i\boldsymbol{q}\cdot\boldsymbol{r}_j) \tag{3}$$

where i denotes the imaginary unit, $\boldsymbol{r}_j$ is the position of the jth atom in an atomic configuration; f_j is atomic scattering factor of the jth atom and depends on $\boldsymbol{q}$.

For the α → γ phase transformation of RDX at ~4.0 GPa [101,110] (Figs. 4(a) and (b)), we calculate the corresponding single-crystal diffraction patterns with typical synchrotron and XFEL sources. We choose the first harmonic of a synchrotron undulator source (an 18 mm period and 13 mm gap) at the Advanced Photon Source with an 8% bandwidth (Fig. 4(g)). It is noteworthy that the undulator bandwidth is tunable, an advantage for single-crystal diffraction. The single-crystal diffraction patterns (Figs. 4(c) and (d)) display drastic differences upon phase transition. Furthermore, the Q-resolution achievable in these experiments is sufficiently high for partial phase analysis, despite its low symmetry and large unit cells. For an XFEL source with a bandwidth of 0.1%, reasonable single-crystal diffraction patterns can also be obtained (Figs. 4(e) and (f)) for partial phase analysis.

For polycrystalline diffraction, diffraction rings from a deformed specimen carry information on phase and strain, as well as strength. As we demonstrated recently [51], the Singh theory [111] can be used to deduce volumetric strain and residual strength from diffraction rings obtained with a properly designed diffraction–detection geometry.

The geometry in Fig. 5(a) can be considered as an example of dynamic XRD under shock compression. ψ represents the angle between the diffraction plane normal and the loading direction and can be calculated from the diffraction and azimuthal angles. The distribution of ψ on a 2D diffraction detector is shown in Fig. 5(b). Furthermore, the lattice spacing $d_m(hkl)$ extracted from a 2D diffraction pattern with Bragg's law, is related to ψ via

$$d_m(hkl) = d_P(hkl)\left[1 + \left(1 - 3\cos^2\psi\right)Q(hkl)\right] \tag{4}$$

where, $d_P(hkl)$ denotes d-spacing for a specific diffraction plane (hkl) due to equivalent hydrostatic stress and Q depends on strength,

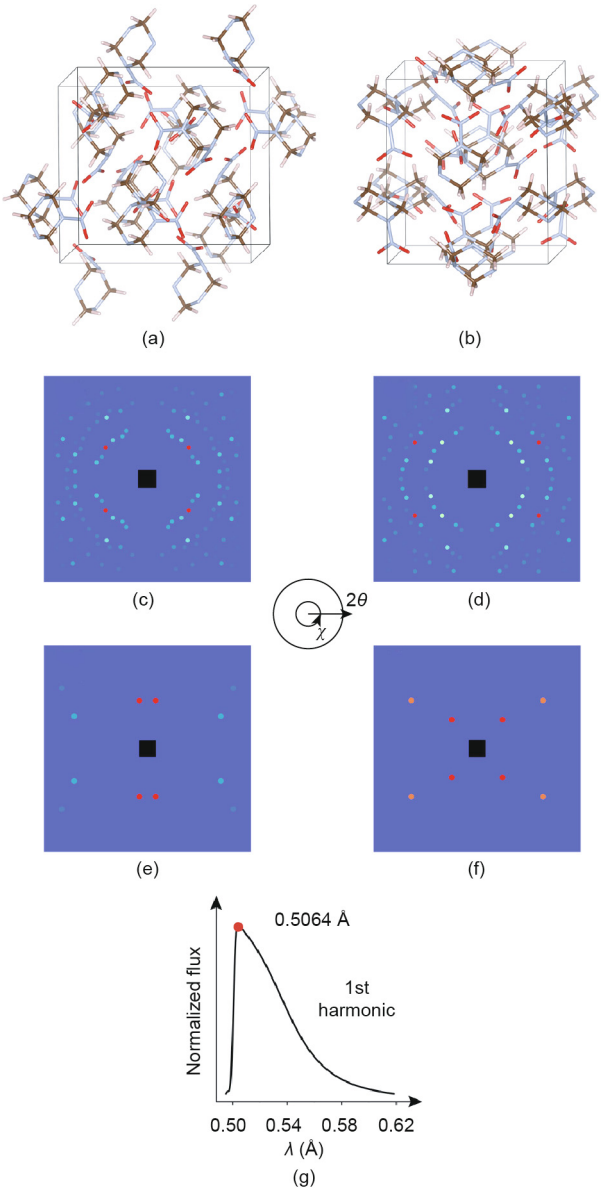

Fig. 4. Single-crystal XRD measurements on shock-compressed RDX with single-bunch synchrotron and XFEL sources (simulated). (a) Crystal structure of α-RDX [107]. (b) Crystal structure of γ-RDX [102]. 2D XRD patterns for a "pink" synchrotron source (c) and (d) and for an XFEL source (e) and (f) of α-RDX and γ-RDX, respectively. Here, 2θ represents the diffraction angle and χ is the azimuthal angle of the diffraction vector projected on the diffraction pattern. (g) A representative undulator X-ray spectrum, where λ means the wavelength of X-ray. XFEL: 22.68 keV, 0.1% bandwidth (BW).

residual strength, and single-crystal elastic compliances. The residual strength t is given by $t = 6G\langle Q(hkl)\rangle f$, where G is the aggregate shear modulus, and parameter f is approximately 1 for all crystal systems.

A polycrystalline α-RDX sample is compressed uniaxially by 5% to mimic plate impact under the loading–diffraction–detection geometry in Fig. 5(a), and the corresponding diffraction patterns before and after shock compression are presented in Figs. 5(c) and (d), respectively. Fitting the diffraction rings at ambient condition yields $Q = 0$, leading to zero residual strength and volumetric strain, as expected. For the diffraction pattern during shock compression, the residual strength is obtained as t = 0.88 GPa with shear modulus G = 7.83 GPa [112], and the volumetric strain is 5% as preset. Thus, the Singh method can be used to obtain the volumetric strain and residual strength during shock compression, as demonstrated for metals [51].

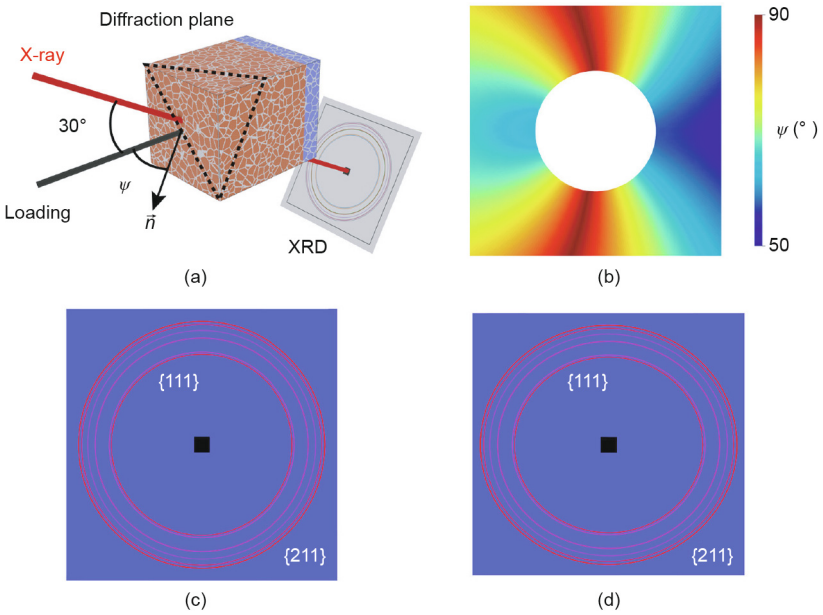

Fig. 5. XRD measurements on shock-compressed polycrystalline RDX with 25 keV monochromatic X-rays (simulated). (a) Loading and diffraction geometries of ψ, the angle between the shock direction and the normal of a specific diffracting plane ($\vec{n}$). (b) Distribution of ψ on the 2D diffraction detector, set perpendicular to the incident X-ray beam. XRD patterns of (c) uncompressed and (d) 5%-compressed α-RDX.

2.3.2. CDI

Single grains or single particles represent the smallest structural component of EMs, and their size, shape, and internal defects can affect the performance of EMs significantly [113]. For example, the "grain size effect" on the shock sensitivity of high explosives has been extensively studied [114]. There have been attempts to lower the shock sensitivity by reducing crystal defects [115,116]. Resolving the single-particle structure and dynamics is directly relevant to the synthesis, processing, and performance of EMs [113,117].

Coherent XRD imaging techniques, especially Bragg CDI (BCDI) and plane-wave CDI (PCDI), are a set of novel X-ray microscopy tools capable of sub-nanometer- and nanometer-level spatial resolutions [118,119]. BCDI is used to investigate the 3D Bragg node of a single-crystal grain via slightly rotating the grain (Fig. 6(a)), and can resolve its 3D structure, 3D strain, and internal defects, including twinning and dislocations [119–122]. Scattering intensity $I(\boldsymbol{q})$ at a given scattering vector $\boldsymbol{q}$ near a Bragg node can be written as

$$I(\boldsymbol{q}) = \left| \int_0^\infty \rho_{\mathrm{L}}(\boldsymbol{r}) s(\boldsymbol{r}) \mathrm{e}^{i\boldsymbol{q}\cdot\boldsymbol{r}} \mathrm{e}^{i\boldsymbol{q}\cdot\boldsymbol{u}(\boldsymbol{r})} \mathrm{d}\boldsymbol{r} \right|^2 \tag{5}$$

where $\rho_{\mathrm{L}}(\boldsymbol{r})$ is electron density of the lattice, $s(\boldsymbol{r})$ is crystal's shape function, and $\boldsymbol{u}(\boldsymbol{r})$ represents the displacement field of atoms compared to their ideal lattice sites. PCDI is intended for reconstructing the structure of an isolated crystalline or non-crystalline particle, via detecting coherently scattered X-rays [123–125] (Fig. 6(b)). Unlike BCDI, scattering intensity $I(\boldsymbol{q})$ for PCDI is determined only by a particle's electron density distribution function, $\rho(\boldsymbol{r})$, and $I(\boldsymbol{q})$ is given by

$$I(\boldsymbol{q}) = \left| \int_0^\infty \rho(\boldsymbol{r}) \mathrm{e}^{i\boldsymbol{q}\cdot\boldsymbol{r}} \mathrm{d}\boldsymbol{r} \right|^2 \tag{6}$$

Although CDI has rarely been applied to EMs, it does exhibit unique potential. Single grains investigated by BCDI can either be isolated, within a polycrystalline assembly, or embedded in a polymeric matrix (such as PBX). For an isolated grain, the information on 3D structure, 3D strain, and internal defects can be obtained. Moreover, the methodology and experimental instrumentation established for inorganic/metallic nanoparticles [126,127] can be applied directly. For a single grain within a polycrystalline assembly or a polymeric matrix, the aforementioned information can be employed to infer the grain–grain and grain–binder interactions. Grain responses and defect dynamics under external loading can also be derived by *in situ* BCDI measurements, as presented in Refs. [119,128]. Considering the complexity imposed by the BCDI experiments on EMs, advanced simulation tools, such as GAPD [108] become crucial for experimental design and data interpretation. Fig. 6(b) shows a 3D Bragg node of a Cu nanorod, calculated with GAPD. Its internal twinning defect can be well-reconstructed (Fig. 6(c)). BCDI may not be realistic for high-speed or ultrafast measurements, because of the requirement of sample rotation. Moreover, the brilliance of the incident X-rays is severely limited to mitigate radiation damage to an EM specimen [129].

With intense femtosecond X-ray pulses from an XFEL, single-shot PCDI has been demonstrated to be capable of resolving transient nanoscale dynamics with ~10 fs temporal resolution [125]. Fig. 6(d) presents a PCDI pattern of a bacterium with a single XFEL pulse, and the corresponding reconstructed 2D structure [130]. Explosion dynamics of sucrose nanospheres was studied using single-shot PCDI, and significant sample expansion was observed at 500 fs–1 ps after pump [131]. Given the similarity between sucrose and organic explosives [132], such measurements can be extended to EMs. The pump can either be an optical laser or an X-ray pulse from XFEL. For the X-ray pump and probe with the split-and-delay scheme, the first X-ray pulse can be used for ignition and the simultaneous structural analysis of a particle, while the second X-ray pulse can probe the ignition/explosion dynamics at a certain delay [131]. Such experiments enable us to resolve the growth, combustion or explosion dynamics at the single particle level [113,133–135].

2.3.3. SAXS

Inherent structural heterogeneities (Fig. 7(a)) introduced during manufacturing and processing, ranging from nanometer to micrometer length scales, can have significant impacts on the safety and performance of EMs [141–144]. Moreover,

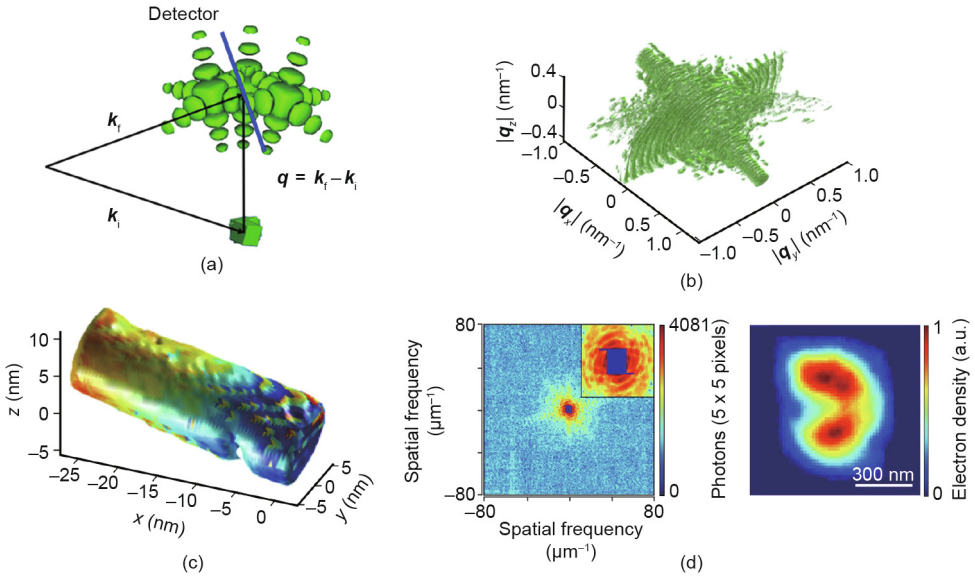

Fig. 6. (a) Schematic diagram of CDI. $\boldsymbol{k}_i$ and $\boldsymbol{k}_f$ are the incident and diffracted X-ray wavevectors, respectively. $\boldsymbol{q}$ represents the diffraction wavevector. (b) Simulated reciprocal space of a Cu sample with a single twin. $\boldsymbol{q}_x$, $\boldsymbol{q}_y$ and $\boldsymbol{q}_z$ are three basic vectors of reciprocal space. (c) Reconstruction of (b). (d) Representative diffraction pattern and reconstructed image of *Staphylococcus aureus*. (d) Reproduced from Ref. [130] with the permission of Springer Nature, ©2016.

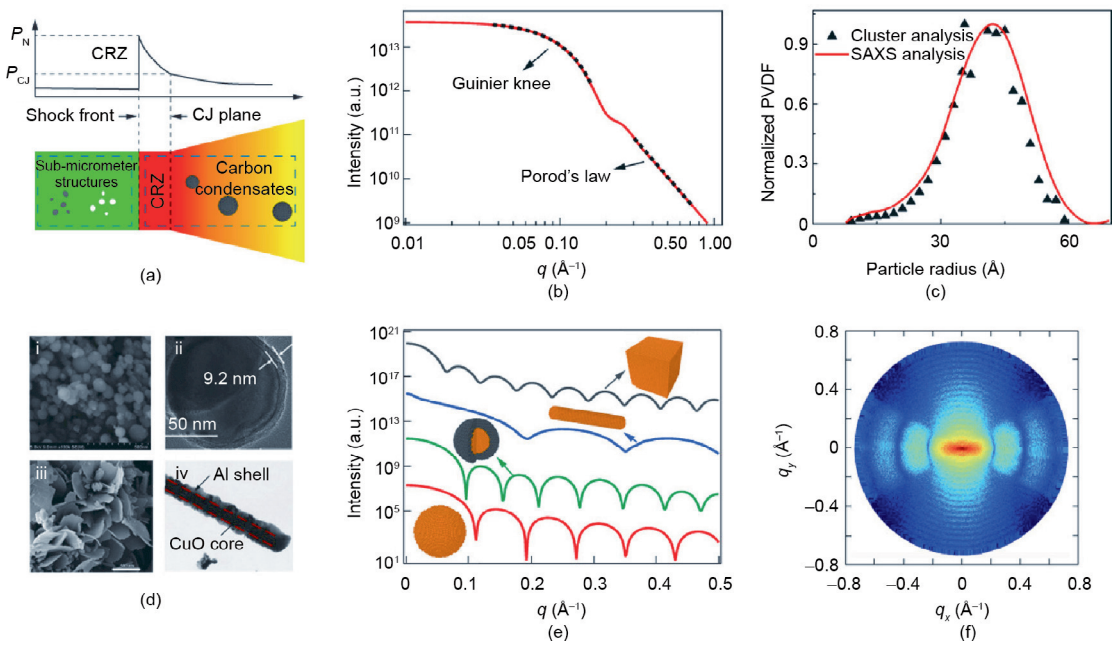

Fig. 7. Resolving structural inhomogeneities and dynamics of EMs with SAXS measurements. (a) Schematic diagram of a detonation model, and corresponding sub-micrometer structures of both initial explosives and detonation products. The chemical decomposition of an explosive occurs in the chemical reaction zone (CRZ). P_N and P_{CJ} denote the peak pressure and pressure at the Chapman–Jouguet (CJ) plane where the chemical reaction ceases, respectively. (b) Guinier approach and Porod's law for obtaining the sizes and surface areas of particles/voids, respectively. (c) Particle/void size distribution function (PVDF) derived using scattering profile fitting methods. (d) Typical morphologies of nanoEMs. (e) SAXS curves of different nanostructures. (f) Anisotropic SAXS pattern of a dense system consisting of nanorods with preferred orientations. (c) Reproduced from Ref. [136] with the permission of the International Union of Crystallography, ©2019; (d) reproduced from Refs. [137–140] with the permission of Elsevier, ©2016, ©2020, ©2017, and ©2017, respectively.

nanostructures can be formed as a denotation product. For example, solid carbon is believed to be generated as a major constituent of the detonation products of carbon-rich high explosives (Fig. 7(a)) [145–147]. Characterizing such nanostructures initially or during dynamic loading (their formation and growth dynamics) is essential to establish structure–property relations and understanding the physical and chemical mechanisms in EMs.

SAXS is sensitive to electron density variations or contrast across length scales ranging between a few nanometers to micrometers, and is well-suited for the structural characterization of EMs at these scales. Abundant information can be obtained non-destructively from SAXS measurements, such as particle size distributions (monodisperse or polydisperse) and pore morphologies (open or closed). For monodisperse systems consisting of particles

or voids with contrast $\Delta\rho$, the radius of gyration R_g and surface area S can be obtained via the Guinier approach

$$I(q) = I(0)\exp\left(-q^2R_g^2/3\right) \quad (7)$$

and the Porod's law

$$I(q) \approx 2\pi(\Delta\rho)^2 q^{-4} S \quad (8)$$

respectively (Fig. 7(b)). Here, I is scattering intensity and q is the modulus of the scattering vector. For polydisperse systems, particle size distributions can be obtained by curve fitting (Fig. 7(c)).

SAXS has been successfully applied to obtain the surface areas and the internal void and particle size distributions for the powders and pressed pellets of high explosives [148]. For example, synchrotron-based *in situ* SAXS measurements revealed that thermal cycling leads to a larger void size and higher void concentration in 1,3,5-triamino-2,4,6-trinitrobenzene (TATB)-based PBXs [149], and can be seen as an application in PBX manufacturing. Highly brilliant advanced light sources also enable us to investigate highly transient processes [46,150]. Time-resolved SAXS (TR-SAXS), based on synchrotron or XFEL sources is promising to answer certain unresolved questions, especially those that cannot be addressed due to their highly transient nature and the lack of an appropriate diagnostic tool. For instance, synchrotron-based pink-beam TR-SAXS measurements were conducted to explore the mechanism of formation of carbon condensation following detonation [151–153], and the feasibility of pink-beam SAXS was demonstrated [154]. Recent studies indicate that diamond particles form and grow slightly within 300 ns after detonation [155,156], although it is desirable to combine TR-SAXS with simultaneous dynamic XRD to investigate processes discussed above.

Nanoenergetic materials (nanoEMs) represent an interesting group of EMs with high energy density and excellent combustion performance [134,157,158]. NanoEMs can assume various morphologies (Fig. 7(d)), such as nanospheres [159], nanorods/nanowires [160], networks [161], nanolayers [162], and core–shell structures [163,164]. SAXS is also advantageous in characterizing these nanostructures (Fig. 7(e)), including particle size distribution and nanorod radius. It is worth mentioning that the interpretation of SAXS measurements can benefit greatly from advanced simulation tools, such as SLADS [165] and GAPD, particularly for nanostructures that cannot be simulated or modeled with traditional simulation/analysis methods. These two codes are capable of calculating the scattering of large, anisotropic, and dense nanoparticle systems. Fig. 7(f) illustrates a simulated anisotropic SAXS pattern for a dense system consisting of nanorods with preferred orientations.

2.4. Simultaneous multiscale measurements

With many physical and chemical processes in EMs being multiscale in nature, it is highly desirable to obtain information at multiple spatial scales simultaneously during a single shot. In principle, separate "identical" shots can be conducted to acquire data at different spatial scales. However, in reality, no two shots are identical. The approach of simultaneous multiscale measurements is particularly advantageous in experimental rigor, and can bridge measurements at different scales and reveal the physics across different spatial scales.

Three main types of X-ray diagnostics, namely, imaging and diffraction/scattering (Fig. 1(a)), can be implemented simultaneously through a combination of two or three types, such as XRD + PCI and XRD + SAXS, to obtain information at the micro- and mesoscales. In addition, conventional bulk-scale techniques, such as laser interferometry and strain or stress gauges, can be utilized for macroscale measurements. Therefore, in principle, micro-, meso-, and macroscale measurements can be performed during a single shot. Here, microscale can be broadly defined to include lattice and nanoscale.

For the XRD + PCI measurements, microscale (lattice-level) and mesoscale (in terms of strain field, for instance) information can be acquired with XRD and PCI, respectively. For example, this technique was applied to a textured magnesium alloy AZ31 [57,166]; XRD indicates the presence/absence of deformation twinning, whereas PCI demonstrates strain localization/delocalization, and the stress–strain curves (obtained from stress gauges) exhibit different strain rate hardening features. Such simultaneous multiscale measurements revealed rigorously for the first time that deformation twinning induces strain delocalization, which in turn leads to increased strain rate hardening in magnesium alloy AZ31. The simultaneity allows for sensible cross-scale connections to be made and the underlying physics to be revealed. The XRD + SAXS measurements are helpful in obtaining the phase and size information of nanoparticles simultaneously, and can be used to understand, for instance, the phase, size, and dynamics of post-detonation carbon condensates. Furthermore, the simultaneous multiscale measurements are expected to be applicable to EMs.

3. Dynamic THz and optical diagnostics

3.1. THz and optical spectroscopy

The THz regime is located between the microwave and mid-infrared regimes on the electromagnetic spectrum [47], spanning 0.3–10 THz (or 10–300 cm^{-1}). Certain vibrational modes of EMs can generate unique THz spectral features, thus being useful in the detection and identification of EMs [168]. Additionally, THz spectroscopy can yield the absorption coefficients and refractive indices of EMs [169]. Furthermore, minor changes in the molecular configurations of EMs may result in THz spectral changes. Consequently, THz spectroscopy can reflect the dynamic chemical and physical responses of EMs to external stimuli.

Recently, the THz spectroscopy of EMs has been extended to low temperatures [170,171]. For example, Fig. 8(a) illustrates the temperature-dependent THz absorption spectra of single-crystal RDX measured along the [002] direction using THz time domain spectroscopy (THz-TDS) at 77–300 K. When the temperature increases to approximately 200 K, the absorption peaks of RDX around 0.5 THz disappear, indicating a possible phase change. Melinger et al. [170] measured the THz absorption spectra of RDX films with THz-TDS at 13–293 K. Below 80 K, there are more than 10 THz absorption peaks. At 80–293 K, the spectra show only one distinct peak at approximately 0.84 THz, which becomes relatively weak and broadened as the temperature increases. In Fig. 8(a), the absorption peaks at around 0.5 THz weaken and then disappear for single-crystal RDX along the [002] direction. Damarla et al. [172] reported the THz absorption of RDX powders in a Teflon matrix measured using THz-TDS at 303–573 K. With increasing temperature, the THz absorption peaks of RDX at approximately 0.84 THz broaden at 378 K, indicating thermally initiated decomposition.

Although THz absorption spectroscopy has been explored for molecular crystals under static compression [173], it has not been explored under dynamic loading. As a linear absorption spectroscopy technique, the detection sensitivity of THz absorption spectroscopy should be considerably higher than those of nonlinear optical spectroscopy techniques, such as coherent anti-Stokes Raman spectroscopy (CARS) and Raman spectroscopy [174]; thus, THz absorption spectroscopy demonstrates a significant potential in investigating EMs under shock compression.

Optical spectroscopy has long been used to study dynamic chemical and physical processes in EMs, particularly owing to its

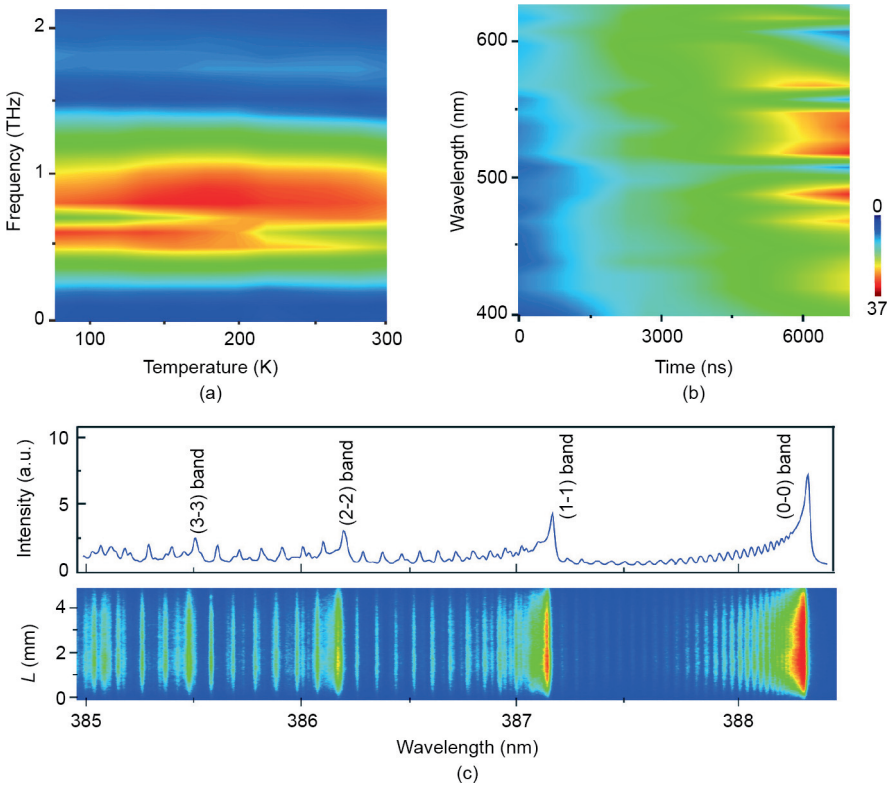

Fig. 8. (a) Temperature-dependent THz absorption spectroscopy of RDX along [002]. (b) Spectral radiation in $GW \cdot m^{-3} \cdot Sr^{-1}$ from shocked methane diluted in Ar. (c) Emission spectra of CN molecules from laser-ablated nitromethane in an Ar atmosphere. *L* denotes the longitudinal position. (c) Reproduced from Ref. [167] with the permission of Elsevier, ©2020.

high temporal resolutions [175]. Ultrafast optical absorption and Raman spectroscopy, including UV/visible absorption spectroscopy [176], infrared absorption spectroscopy [177], Raman spectroscopy [178], and CARS [179,180], can achieve temporal resolutions up to the probe laser pulse width (the shortest of which can be tens of femtoseconds). In contrast, ultrafast emission spectroscopy, including optical pyrometry and LIBS, can achieve temporal resolution limits of ultrafast detectors, such as streak cameras (1–100 ps) [181,182] and photomultiplier tubes (sub-nanoseconds).

For pyrometry based on photomultiplier tubes, spectral radiation is captured at different wavelengths (channels), and such emission spectra are frequently used to deduce the shock temperature from Planck's law with temperature or wavelength dependent emissivity [32]. Fig. 8(b) depicts the spectral radiation of shocked gas-phase methane diluted in Ar measured with a 40-channel optical pyrometer; the onset of intense emission at ~4500 ns indicates an ignition event.

Bouyer et al. [183] captured the SDT of nitromethane within a few nanoseconds using a 16-channel pyrometer. Different stages of the SDT, were clearly observed including shock entrance, super-detonation, strong detonation, and steady detonation.

In LIBS, a pulsed laser is focused onto a specimen and ablates it, creating a microplasma for emission spectroscopy. On the basis of molecular and atomic emission lines, LIBS has been mostly utilized in identifying and detecting EMs [184,185]. To improve the sensitivity and selectivity of LIBS, double nanosecond-laser pulses [186] or femtosecond-laser pulses [187] are also used. Time-resolved LIBS has been attempted to understand chemical reaction mechanisms of EMs during laser ablation [185,188,189]. Recently, Zhao et al. [167] investigated atomic and molecular emission of nitromethane in an Ar or N_2 buffer gas using fs LIBS. They identified electronic bands of CN, C_2, and NH molecules and atomic transition lines of CI, NI, and Hα (Fig. 8(c)). Rotational and vibrational temperatures of CN molecules were determined assuming local thermodynamic equilibrium [191], via fitting with the following equation:

$$I_{n',n'',v',v'',J',J''} = C_e \frac{q_{v',v''} S_{J',J''}}{Q_{rot} v'} \tilde{\nu}^4_{J',J''} \exp\left(-\frac{F'hc}{k_B T_{rot}}\right) \exp\left(-\frac{G'hc}{k_B T_{vib}}\right) \quad (9)$$

where, *I* is emission intensity; *n*, *v*, and *J* are principal, vibrational, and rotational quantum numbers, respectively; C_e is the emission constant; *h*, *c*, and k_B are Planck's constant, the vacuum light velocity, and Boltzmann constant, respectively; $\tilde{\nu}_{J',J''}$ is the transition wavenumber; T_{rot} and T_{vib} are rotational and vibrational temperatures, respectively; Q_{rot} is the rotational partition function; $q_{v',v''}$ and $S_{J'J''}$ are the Franck–Condon coefficient and the Hönl–London factor, respectively; and F' and G' are the rotational and vibrational energy, respectively.

Since LIBS detects only a very small number of atoms and molecules, its capability can be expanded with sensitive trace gas techniques such as mass spectrometry [190]. For example, Civiš et al. [190] studied 1,1-diamino-2,2-dinitroethylene (FOX-7) using a combination of LIBS and selected ion flow tube mass spectrometry (SIFT-MS). Twelve stable gaseous compounds formed in a laser-induced microplasma were identified by SIFT-MS; C, H, and N atoms and CN, OH, and NO molecules were detected via LIBS. The decomposition mechanism in laser-induced breakdown of FOX-7 was then proposed on the basis of the joint measurements.

Rapid expansion of laser-induced microplasma can generate shock waves, which interrupt molecular formation in a microplasma [31]. For example, Harilal et al. [31] investigated the molecular formation mechanism in laser-ablated aluminum with shock wave generated at the plasma front. At the early stage of the plasma expansion, the shock wave inhibited the combustion

process by keeping the ambient oxygen away from the microplasma. After the shock wave collapsed, the molecular formation became prevalent. Using a streak camera, Hori et al. [191] obtained time-resolved, single-shot LIBS spectra from a laser induced microplasma in air. Rabasovic et al. [192] tracked the maximum brightness displacement during the rapid plasma expansion of a laser-induced microplasma in air, and a velocity of plasma expansion of 35 $km \cdot s^{-1}$ was obtained using streaked LIBS. Therefore, LIBS has the potential for investigation of EMs under laser ablation.

3.2. Ultrafast imaging interferometry

Ultrafast imaging interferometry allows for temporally and spatially resolved (1D or 2D) measurements of displacement/velocity fields under dynamic loading and is advantageous for making connections between structural inhomogeneity and wave front roughening, and likely, hot spots. Such interferometric diagnostics include 1D line-VISAR [193], 2D-VISAR [194], and TIDI [195]. TIDI/2D-VISAR maps out-of-plane surface (or interface) displacement/velocity field, and their highest temporal resolution can reach the width of a probe laser pulse or the temporal resolution limit of a detector (femtoseconds to nanoseconds) [196,197]. The spatial resolution is normally 1–10 μm. The displacement sensitivity of TIDI and velocity sensitivity of VISAR are approximately 10 nm and 10 ms^{-1}, respectively.

The probe and reference light paths (two arms) are built in a TIDI system, and the phase of the probe light evolves dynamically as a specimen responds to an external stimulus. The interference of these two arms is recorded by a 2D detector as

$$I(x, y) = [1 + r^2(x, y)] + 2r(x, y)\cos[2\pi f_0 x + \Phi(x, y)], \quad (10)$$

where I is light intensity, r is the reflection coefficient, f_0 is the initial frequency of fringes, and Φ is the phase shift induced by the loading. The displacement field can be obtained via solving Φ, as follows:

$$d(x, y) = \frac{\lambda_0}{4\pi\cos\theta}\Phi(x, y)$$

where λ_0 is the wavelength of the probe light and θ is tilt angle in the incident light. For 2D-VISAR, both paths collect lights from the same target, and an etalon is placed in the reference path to induce a time delay.

TIDI and 2D-VISAR have been used in dynamic loading of metals, and these successful applications spell their potential for EMs. Fig. 9(a) shows a TIDI fringe image and corresponding displacement field of polycrystalline materials under shock loading [198]. The out-of-plane displacement field shows displacement gradients and thus wave field heterogeneity, as a result of slight bowing in loading (the general tendency) and local grain structure (the local fluctuations). TIDI is a promising tool for studying the effect of structural inhomogeneity on shock response of EMs, in particular, thermomechanical processes related to hot spots.

With a streak camera, line-VISAR is capable of measuring velocity field across a line by recording Doppler shift in the frequency of a probe laser. The interferometer consists of two light paths, and an etalon is placed in one of the paths. The time delay induced by the etalon creates phase shift between the two paths. Typical temporal, spatial, and velocity resolutions of line-VISAR are 1 ns, 10 μm, and 20 ms^{-1}, respectively. An example of line-VISAR measurement for laser-shocked aluminum [199] is shown in Fig. 9(b). Here, line-VISAR measures the free surface velocity field (1D) and shock front roughening. Although the roughening is minor in this case, the high spatial and temporal resolutions offered by line-VISAR allow for ultrafast measurements on wave front inhomogeneity in EMs (such as PBX) with inherent structural inhomogeneity at different spatial scales.

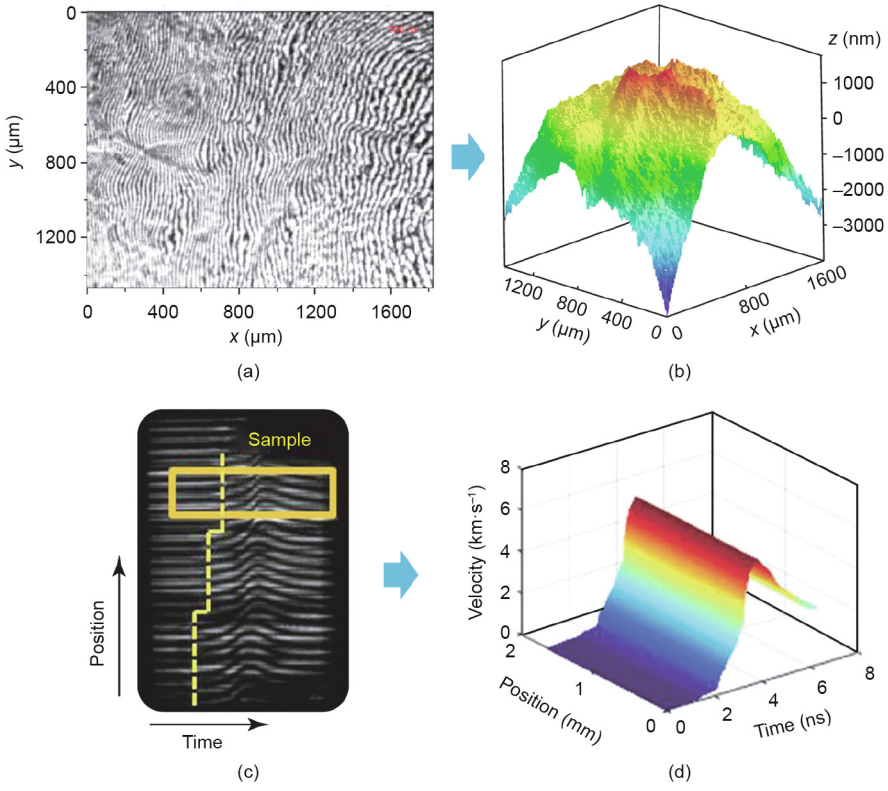

Fig. 9. Dynamic imaging interferometry. (a) TIDI: fringe pattern of shocked copper and (b) corresponding out-of-plane displacement map. (c) Line-imaging VISAR: streak camera record of laser-shocked aluminum and (d) corresponding velocity history. (a, b) Reproduced from Ref. [198] with the permission of AIP Publishing, ©2007; (c, d) reproduced from Ref. [199] with the permission of Spring Nature, ©2019.

4. Summary

We briefly review X-ray, THz, and optical diagnostics for investigating EMs at multiple temporal and spatial scales, including 2D and 3D X-ray imaging, X-ray diffraction, coherent XRD imaging, SAXS, THz and optical absorption/emission spectroscopy, and 1D and 2D velocity/displacement interferometry, with emphasis on their capabilities for temporally and/or spatially resolved measurements. Basic principles of measurement and data analysis and illustrative examples are presented. In general, the discussed techniques have great potential for application in investigation of EMs, and there is a requirement for concerted efforts in defining scientific questions and engineering problems, experimental design, data analysis and interpretation, and multiscale modeling.

Acknowledgements

We are grateful for contributions from the PIMS X-ray Group. This work was supported by National Natural Science Foundation of China (11627901 and 11802252).

Compliance with ethics guidelines

Yiyang Zhang, Sen Chen, Yang Cai, Lei Lu, Duan Fan, Jinchun Shi, Junyu. Huang, and Sheng-Nian Luo declare that they have no conflict of interest or financial conflicts to disclose.

References

[1] Rice BM. Overview of research in energetic materials. In: Politzer P, Murray JS, editors. Energetic materials: Part 1. Decomposition, crystal and molecular properties. Amsterdan: Elsevier; 2003. p. 1–3.
[2] Manaa MR. Initiation and decomposition mechanisms of energetic materials. In: Politzer P, Murray JS, editors. Energetic materials: Part 2. Detonation, combustion. Amsterdan: Elsevier; 2003. p. 71–100.
[3] Badgujar DM, Talawar MB, Asthana SN, Mahulikar PP. Advances in science and technology of modern energetic materials: an overview. J Hazard Mater 2008;151(2–3):289–305.
[4] Zhang W, Zhang J, Deng M, Qi X, Nie F, Zhang Q. A promising high-energy-density material. Nat Commun 2017;8(1):1–7.
[5] Agrawal JP. High energy materials: propellants, explosives and pyrotechnics. Hoboken: John Wiley and Sons Ltd.; 2010.
[6] Handley CA, Lambourn BD, Whitworth NJ, James HR, Belfield WJ. Understanding the shock and detonation response of high explosives at the continuum and meso scales. Appl Phys Rev 2018;5(1):011303.
[7] Bennett JG, Haberman KS, Johnson JN, Asay BW. A constitutive model for the non-shock ignition and mechanical response of high explosives. J Mech Phys Solids 1998;46(12):2303–22.
[8] Dlott DD. New developments in the physical chemistry of shock compression. Annu Rev Phys Chem 2011;62(1):575–97.
[9] Yeager JD, Luo SN, Jensen BJ, Fezzaa K, Montgomery DS, Hooks DE. High-speed synchrotron X-ray phase contrast imaging for analysis of low-Z composite microstructure. Compos Part A Appl S 2012;43(6):885–92.
[10] Smirnov E, Muzyrya A, Kostitsyn O, Badretdinova LC, Ten K, Pruuel E, et al. Investigation of micro-, meso-, and macrostructure of the condensed heterogeneous explosives using synchrotron radiation. Bull Russ Acad Sci Phys 2015;79(1):20–5.
[11] Liu Y, Xu J, Huang S, Li S, Wang Z, Li J, et al. Microstructure and performance of octahydro-1,3,5,7-tetranitro-1,3,5,7-tetrazocine (HMX) crystal clusters obtained by the solvation-desolvation process. J Energy Mater 2019;37(3):282–92.
[12] Zhang J, Jackson TL. Effect of microstructure on the detonation initiation in energetic materials. Shock Waves 2019;29(2):327–38.
[13] Field JE. Hot spot ignition mechanisms for explosives. Acc Chem Res 1992;25(11):489–96.
[14] Field JE, Bourne NK, Palmer SJP, Walley SM. Hotspot ignition mechanisms for explosives and propellants. Philos Trans R Soc London Ser A Phys Eng Sci 1992;339(1654):269–83.
[15] An Q, Zybin SV, Goddard WA, Jaramillo-Botero A, Blanco M, Luo SN. Elucidation of the dynamics for hot-spot initiation at nonuniform interfaces of highly shocked materials. Phys Rev B Condens Matter Mater Phys 2011;84(22):220101.
[16] You S, Chen MW, Dlott DD, Suslick KS. Ultrasonic hammer produces hot spots in solids. Nat Commun 2015;6(1):6581.
[17] Halfpenny PJ, Roberts KJ, Sherwood JN. Dislocations in energetic materials. J Mater Sci 1984;19(5):1629–37.
[18] Cawkwell MJ, Ramos KJ, Hooks DE, Sewell TD. Homogeneous dislocation nucleation in cyclotrimethylene trinitramine under shock loading. J Appl Phys 2010;107(6):063512.
[19] Ciezak JA, Jenkins TA. The low-temperature high pressure phase diagram of energetic materials: I. hexahydro-1,3,5-trinitro-*s*-triazine. Propell Explos Pyrot 2008;33(5):390–5.
[20] Willey TM, Lauderbach L, Gagliardi F, Van Buuren T, Glascoe EA, Tringe JW, et al. Mesoscale evolution of voids and microstructural changes in HMX-based explosives during heating through the $\beta-\delta$ phase transition. J Appl Phys 2015;118(5):055901.
[21] Adams GF, Shaw Jr RW. Chemical reactions in energetic materials. Annu Rev Phys Chem 1992;43(1):311–40.
[22] Shaw MS, Johnson JD. Carbon clustering in detonations. J Appl Phys 1987;62(5):2080–5.
[23] Greiner NR, Phillips DS, Johnson JD, Volk F. Diamonds in detonation soot. Nature 1988;333(6172):440–2.
[24] Ye S, Koshi M. Theoretical studies of energy transfer rates of secondary explosives. J Phys Chem B 2006;110(37):18515–20.
[25] Ye SJ, Tonokura K, Koshi M. Energy transfer rates and impact sensitivities of crystalline explosives. Combust Flame 2003;132(1–2):240–6.
[26] Tokmakoff A, Fayer MD, Dlott DD. Chemical reaction initiation and hot-spot formation in shocked energetic molecular materials. J Phys Chem 1993;97(9):1901–13.
[27] Fried LE, Ruggiero AJ. Energy transfer rates in primary, secondary, and insensitive explosives. J Phys Chem 1994;98(39):9786–91.
[28] McNesby KL, Coffey CS. Spectroscopic determination of impact sensitivities of explosives. J Phys Chem B 1997;101(16):3097–104.
[29] Bourne NK, Milne AM. Shock to detonation transition in a plastic bonded explosive. J Appl Phys 2004;95(5):2379–85.
[30] Rethfeld B, Sokolowski-Tinten K, Von Der Linde D, Anisimov S. Timescales in the response of materials to femtosecond laser excitation. Appl Phys A Mater Sci Process 2004;79(4–6):767–9.
[31] Harilal SS, Brumfield BE, Cannon BD, Phillips MC. Shock wave mediated plume chemistry for molecular formation in laser ablation plasmas. Anal Chem 2016;88(4):2296–302.
[32] Luo SN, Akins JA, Ahrens TJ, Asimow PD. Shock compressed $MgSiO_3$ glass, enstatite, olivine, and quartz: optical emission, temperatures, and melting. J Geophys Res 2004;109:B05205.
[33] Chen P, Huang F, Dai K, Ding Y. Detection and characterization of long-pulse low-velocity impact damage in plastic bonded explosives. Int J Impact Eng 2005;31(5):497–508.
[34] Hooks DE, Ramos KJ, Martinez AR. Elastic-plastic shock wave profiles in oriented single crystals of cyclotrimethylene trinitramine (RDX) at 2.25 GPa. J Appl Phys 2006;100(2):024908.
[35] Parab ND, Roberts ZA, Harr MH, Mares JO, Casey AD, Gunduz IE, et al. High speed X-ray phase contrast imaging of energetic composites under dynamic compression. Appl Phys Lett 2016;109(13):131903.
[36] Zhao PD, Lu FY, Lin YL, Chen R, Li JL, Lu L. Technique for combined dynamic compression-shear testing of PBXs. Exp Mech 2012;52(2):205–13.
[37] Shi JC, Shang YL, Ye W, Zhang RT, Luo SN. Shock-tube experiments and chemical kinetic modeling study of CH_4 sensitized by CH_3NHCH_3. Energy Fuels 2018;32(4):5588–95.
[38] Shang YL, Shi JC, Ning HB, Zhang RT, Wang HY, Luo SN. Ignition delay time measurements and kinetic modeling of CH_4 initiated by CH_3NO_2. Fuel 2019;243:288–97.
[39] Wang X, Wu Y, Huang F. Thermal–mechanical–chemical responses of polymer-bonded explosives using a mesoscopic reactive model under impact loading. J Hazard Mater 2017;321(806):256–67.
[40] Oswald ID, Millar DI, Davidson AJ, Francis DJ, Marshall WG, Pulham CR, et al. High-pressure structural studies of energetic compounds. High Press Res 2010;30(2):280–91.
[41] Funk DJ, Calgaro F, Averitt RD, Asaki MLT, Taylor AJ. THz transmission spectroscopy and imaging: application to the energetic materials PBX 9501 and PBX 9502. Appl Spectrosc 2004;58(4):428–31.
[42] Federici JF, Schulkin B, Huang F, Gary D, Barat R, Oliveira F, et al. THz imaging and sensing for security applications—explosives, weapons and drugs. Semicond Sci Technol 2005;20(7):S266–80.
[43] Hua C, Zhang PJ, Lu XJ, Huang M, Dai B, Fu H. Research on the size of defects inside RDX/HMX crystal and shock sensitivity. Propell Explos Pyrot 2013;38(6):775–80.
[44] Van der Heijden AEDM, Bouma RHB. Crystallization and characterization of RDX, HMX, and CL-20. Cryst Growth Des 2004;4(5):999–1007.
[45] Xiao Y, Sun Y, Zhen Y, Guo L, Yao L. Characterization, modeling and simulation of the impact damage for polymer bonded explosives. Int J Impact Eng 2017;103:149–58.
[46] Luo SN, Jensen BJ, Hooks DE, Fezzaa K, Ramos KJ, Yeager JD, et al. Gas gun shock experiments with single-pulse X-ray phase contrast imaging and diffraction at the Advanced Photon Source. Rev Sci Instrum 2012;83(7):073903.
[47] Baxter JB, Guglietta GW. Terahertz spectroscopy. Anal Chem 2011;83(12):4342–68.
[48] Fan D, Lu L, Li B, Qi ML, Eisenstein JC, Zhao F, et al. Transient X-ray diffraction with simultaneous imaging under high strain-rate loading. Rev Sci Instrum 2014;85(11):113902.
[49] Seiboth F, Fletcher LB, McGonegle D, Anzellini S, Dresselhaus-Cooper LE, Frost M, et al. Simultaneous 8.2 keV phase-contrast imaging and 24.6 keV X-ray

diffraction from shock-compressed matter at the LCLS. Appl Phys Lett 2018;112(22):221907.
[50] Brown SB, Gleason AE, Galtier E, Higginbotham A, Arnold B, Fry A, et al. Direct imaging of ultrafast lattice dynamics. Sci Adv 2019;5(3):eaau8044.
[51] Zhang YY, Tang MX, Cai Y, Eisenstein JC, Luo SN. Deducing density and strength of nanocrystalline Ta and diamond under extreme conditions from X-ray diffraction. J Synchrotron Radiat 2019;26(Pt 2):413–21.
[52] Czerski H, Proud WG. Relationship between the morphology of granular cyclotrimethylene-trinitramine and its shock sensitivity. J Appl Phys 2007;102(11):113515.
[53] An Q, Liu Y, Zybin SV, Kim H, Goddard WA. Anisotropic shock sensitivity of cyclotrimethylene trinitramine (RDX) from compress-and-shear reactive dynamics. J Phys Chem C 2012;116(18):10198–206.
[54] Hudspeth M, Sun T, Parab N, Guo Z, Fezzaa K, Luo S, et al. Simultaneous X-ray diffraction and phase-contrast imaging for investigating material deformation mechanisms during high-rate loading. J Synchrotron Radiat 2015;22(1):49–58.
[55] Brennan Brown S, Lee HJ, Nagler B, Galtier E, Xing Z, Gleason A, et al. Density measurements of dynamically-compressed, melting phase silicon via simultaneous *in-situ* X-ray diffraction and X-ray contrast imaging using the LCLS X-ray free electron laser at MEC. In: Proceedings of the 58th Annual Meeting of the APS Division of Plasma Physics; 2016 Oct 31–Nov 4; San Jose, CA, USA; 2016.
[56] Fan D, Huang JW, Zeng XL, Li Y, Eisenstein JC, Huang JY, et al. Simultaneous, single-pulse, synchrotron X-ray imaging and diffraction under gas gun loading. Rev Sci Instrum 2016;87(5):053903.
[57] Lu L, Huang JW, Fan D, Bie BX, Sun T, Fezzaa K, et al. Anisotropic deformation of extruded magnesium alloy AZ31 under uniaxial compression: a study with simultaneous *in situ* synchrotron X-ray imaging and diffraction. Acta Mater 2016;120:86–94.
[58] Snigirev A, Snigireva I, Kohn V, Kuznetsov S, Schelokov I. On the possibilities of X-ray phase contrast microimaging by coherent high-energy synchrotron radiation. Rev Sci Instrum 1995;66(12):5486–92.
[59] Cloetens P, Barrett R, Baruchel J, Guigay JP, Schlenker M. Phase objects in synchrotron radiation hard X-ray imaging. J Phys D Appl Phys 1996;29(1):133–46.
[60] Olinger B. Compacting plastic-bonded explosive molding powders to dense solids. Tech Report. Los Alamos: Los Alamos National Laboratory; 2005. Apr. Report No.:LA-14173.
[61] Paulson SC, Roberts ZA, Sorensen CJ, Kerschen NE, Harr MH, Parab ND, et al. Observation of damage during dynamic compression of production and low-defect HMX crystals in Sylgard® binder using X-ray phase contrast imaging. J Dyn Behav Mater 2020;6(1):34–44.
[62] Kerschen NE, Sorensen CJ, Guo Z, Mares JO, Fezzaa K, Sun T, et al. X-Ray phase contrast imaging of the impact of a single HMX particle in a polymeric matrix. Propell Explos Pyrot 2019;44(4):447–54.
[63] Kerschen NE, Drake JD, Sorensen CJ, Guo Z, Mares JO, Fezzaa K, et al. X-ray phase contrast imaging of the impact of multiple HMX particles in a polymeric matrix. Propell Explos Pyrot 2020;45(4):607–14.
[64] Lu L, Fan D, Bie BX, Ran XX, Qi ML, Parab N, et al. Note: dynamic strain field mapping with synchrotron X-ray digital image correlation. Rev Sci Instrum 2014;85(7):076101.
[65] Huang JY, Lu L, Fan D, Sun T, Fezzaa K, Xu SL, et al. Heterogeneity in deformation of granular ceramics under dynamic loading. Scr Mater 2016;111:114–8.
[66] Wang BR, Sun T, Fezzaa K, Huang JY, Luo SN. Rate-dependent deformation and Poisson's effect in porous titanium. Mater Lett 2019;245:134–7.
[67] Pan B. Recent progress in digital image correlation. Exp Mech 2011;51(7):1223–35.
[68] Wu SY, Bie BX, Fan D, Sun T, Fezzaa K, Feng ZD, et al. Dynamic shear localization of a titanium alloy under high-rate tension characterized by X-ray digital image correlation. Mater Charact 2018;137:58–66.
[69] Bie BX, Huang JY, Su B, Lu L, Fan D, Eisenstein JC, et al. Dynamic tensile deformation and damage of B_4C-reinforced Al composites: time-resolved imaging with synchrotron X-rays. Mater Sci Eng A 2016;664:86–93.
[70] Li HY, Chai HW, Xiao XH, Huang JY, Luo SN. Fractal breakage of porous carbonate sand particles: microstructures and mechanisms. Powder Technol 2020;363:112–21.
[71] Bie BX, Huang JY, Fan D, Sun T, Fezzaa K, Xiao XH, et al. Orientation-dependent tensile deformation and damage of a T700 carbon fiber/epoxy composite: A synchrotron-based study. Carbon 2017;121:127–33.
[72] Chai HW, Xie ZL, Xiao XH, Xie HL, Huang JY, Luo SN. Microstructural characterization and constitutive modelling of deformation of closed-cell foams based on *in situ* X-ray tomography. Int J Plast 2020;131:102730.
[73] Sjödahl M, Siviour CR, Forsberg F. Digital volume correlation applied to compaction of granular materials. Procedia IUTAM 2012;4:179–95.
[74] Zhang WB, Huang H, Tian Y, Dai B. Characterization of RDX-based thermosetting plastic-bonded explosive by cone-beam microfocus computed tomography. J Energ Mater 2012;30(3):196–208.
[75] Manner VW, Yeager JD, Patterson BM, Walters DJ, Stull JA, Cordes NL, et al. *In situ* imaging during compression of plastic bonded explosives for damage modeling. Materials (Basel) 2017;10(6):638.
[76] Hu Z, Luo H, Bardenhagen SG, Siviour CR, Armstrong RW, Lu H. Internal deformation measurement of polymer bonded sugar in compression by digital volume correlation of *in-situ* tomography. Exp Mech 2015;55(1):289–300.
[77] Yuan ZN, Chen H, Li JM, Dai B, Zhang WB. *In-situ* X-ray tomography observation of structure evolution in 1,3,5-triamino-2,4,6-trinitrobenzene based polymer bonded explosive (TATB-PBX) under thermo-mechanical loading. Materials 2018;11(5):732.
[78] Chen L, Wu L, Liu Y, Chen W. *In situ* observation of void evolution in 1,3,5-triamino-2,4,6-trinitrobenzene under compression by synchrotron radiation X-ray nano-computed tomography. J Synchrotron Radiat 2020;27(Pt 1):127–33.
[79] Yao Y, Chai HW, Li C, Bie BX, Xiao XH, Huang JY, et al. Deformation and damage of sintered low-porosity aluminum under planar impact: microstructures and mechanisms. J Mater Sci 2018;53(6):4582–97.
[80] Pan B, Wu D, Wang Z. Internal displacement and strain measurement using digital volume correlation: a least-squares framework. Meas Sci Technol 2012;23(4):045002.
[81] García-Moreno F, Kamm PH, Neu TR, Bülk F, Mokso R, Schlepütz CM, et al. Using X-ray tomoscopy to explore the dynamics of foaming metal. Nat Commun 2019;10(1):3762.
[82] Baker DR, Brun F, O'Shaughnessy C, Mancini L, Fife JL, Rivers M, et al. A four-dimensional X-ray tomographic microscopy study of bubble growth in basaltic foam. Nat Commun 2012;3(1):1135.
[83] Nommeots-Nomm A, Ligorio C, Bodey A, Cai B, Jones JR, Lee PD, et al. Four-dimensional imaging and quantification of viscous flow sintering within a 3D printed bioactive glass scaffold using synchrotron X-ray tomography. Mater Today Adv 2019;2:100011.
[84] Sloof WG, Pei R, McDonald SA, Fife JL, Shen L, Boatemaa L, et al. Repeated crack healing in MAX-phase ceramics revealed by 4D *in situ* synchrotron X-ray tomographic microscopy. Sci Rep 2016;6(1):23040.
[85] Lu X, Fernández MP, Bradley RS, Rawson SD, O'Brien M, Hornberger B, et al. Anisotropic crack propagation and deformation in dentin observed by four-dimensional X-ray nano-computed tomography. Acta Biomater 2019;96:400–11.
[86] White DJ, Take WA, Bolton MD. Soil deformation measurement using particle image velocimetry (PIV) and photogrammetry. Geotechnique 2003;53(7):619–31.
[87] Parker G, Bourne N, Eastwood D, Jacques S, Dickson P, Lopez-Pulliam I, et al. 4D imaging in thermally damaged polymer-bonded explosives. In: Proceedings of the 20th Biennial Conference of the APS Topical Group on Shock Compression of Condensed Matter; 2017 Jul 9–14; St. Louis, MO, USA; 2017.
[88] Zellner MB, Champley K. Development of a computed tomography system capable of tracking high-velocity unbounded material through a reconstruction volume. Int J Impact Eng 2019;129:26–35.
[89] Walters DJ, Luscher DJ, Yeager JD, Patterson BM. Cohesive finite element modeling of the delamination of HTPB binder and HMX crystals under tensile loading. Int J Mech Sci 2018;140:151–62.
[90] Hu R, Prakash C, Tomar V, Harr M, Gunduz IE, Oskay C. Experimentally-validated mesoscale modeling of the coupled mechanical–thermal response of AP–HTPB energetic material under dynamic loading. Int J Fract 2017;203(1–2):277–98.
[91] Huang JH, Lu SJ, Xie FY, Liu W, Xiao CW, Zhang JJ, et al. Finite element analysis of synergetic deformation in precision cutting of polymer bonded explosive. Mater Des 2020;188:108471.
[92] Harewood FJ, McHugh PE. Comparison of the implicit and explicit finite element methods using crystal plasticity. Comput Mater Sci 2007;39(2):481–94.
[93] Henning GF. Process for making a nitro compound from hexamethylenetetramine. German patent DE 104280; 1899.
[94] Hultgren R. An X-ray study of symmetrical trinitrotoluene and cyclo trimethylenetrinitramine. J Chem Phys 1936;4(1):84.
[95] McCrone WC. Crystallographic data. 32. RDX (cyclotrimethylenetrinitramine). Anal Chem 1950;22(7):954–5.
[96] Miller PJ, Block S, Piermarini GJ. Effects of pressure on the thermal decomposition kinetics, chemical reactivity and phase behavior of RDX. Combust Flame 1991;83(1–2):174–84.
[97] Millar DIA, Oswald IDH, Francis DJ, Marshall WG, Pulham CR, Cumming AS. The crystal structure of β-RDX—an elusive form of an explosive revealed. Chem Commun 2009;7(5):562–4.
[98] Gao C, Yang L, Zeng Y, Wang X, Zhang C, Dai R, et al. Growth and characterization of β-RDX single-crystal particles. J Phys Chem C 2017;121(33):17586–94.
[99] Baer BJ, Oxleyf J, Nicol M. The phase diagram of RDX (hexahydro-1,3,5-trinitro-*s*-triazine) under hydrostatic pressure. High Press Res 1990;2(2):99–108.
[100] Gao C, Zhang X, Zhang C, Sui Z, Hou M, Dai R, et al. Effect of pressure gradient and new phases for 1,3,5-trinitrohexahydro-*s*-triazine (RDX) under high pressures. PCCP 2018;20(21):14374–83.
[101] Goto N, Fujihisa H, Yamawaki H, Wakabayashi K, Nakayama Y, Yoshida M, et al. Crystal structure of the high-pressure phase of hexahydro-1,3,5-trinitro-1,3,5-triazine (γ-RDX). J Phys Chem B 2006;110(47):23655–9.
[102] Davidson AJ, Oswald ID, Francis DJ, Lennie AR, Marshall WG, Millar DI, et al. Explosives under pressure-the crystal structure of γ-RDX as determined by high-pressure X-ray and neutron diffraction. Cryst Eng Comm 2008;10(2):162–5.
[103] Dresselhaus-Cooper LE, Martynowych DJ, Zhang F, Tsay C, Ilavsky J, Wang SG, et al. Pressure-thresholded response in cylindrically shocked cyclotrimethylene trinitramine (RDX). J Phys Chem A 2020;124(17):3301–13.

[104] Ramos K, Addessio FL, Armenta CE, Banesh D, Barber JL, Biwer CM, et al. *In situ* investigation of phase transformation in cyclotrimethylene trinitramine (RDX) during shock loading using X-ray diffraction. Bull Am Phys Soc 2019;64(8).
[105] Turneaure SJ, Sinclair N, Gupta YM. Real-time examination of atomistic mechanisms during shock-induced structural transformation in silicon. Phys Rev Lett 2016;117(4):045502.
[106] Chen S, Li YX, Zhang NB, Huang JW, Hou HM, Ye SJ, et al. Capture deformation twinning in Mg during shock compression with ultrafast synchrotron X-ray diffraction. Phys Rev Lett 2019;123(25):255501.
[107] Choi CS, Prince E. The crystal structure of cyclotrimethylenetrinitramine. Acta Crystallogr B 1972;28(9):2857–62.
[108] E JC, Wang L, Chen S, Zhang YY, Luo SN. GAPD: a GPU-accelerated atom-based polychromatic diffraction simulation code. J Synchrotron Radiat 2018;25(Pt 2):604–11.
[109] Warren BE. X-ray diffraction. New York: Dover Publications; 1990.
[110] Ciezak JA, Jenkins TA, Liu Z, Hemley RJ. High-pressure vibrational spectroscopy of energetic materials: hexahydro-1,3,5-trinitro-1,3,5-triazine. J Phys Chem A 2007;111(1):59–63.
[111] Singh AK. The lattice strains in a specimen (cubic system) compressed nonhydrostatically in an opposed anvil device. J Appl Phys 1993;73(9):4278–86.
[112] Haycraft JJ, Stevens LL, Eckhardt CJ. The elastic constants and related properties of the energetic material cyclotrimethylene trinitramine (RDX) determined by Brillouin scattering. J Chem Phys 2006;124(2):024712.
[113] Huang B, Cao MH, Huang H, Hu CW. Construction and properties of structure- and size-controlled micro/nano-energetic materials. Def Technol 2013;9(2):59–79.
[114] Khasainov B, Ermolaev B, Presles HN, Vidal P. On the effect of grain size on shock sensitivity of heterogeneous high explosives. Shock Waves 1997;7(2):89–105.
[115] Borne L, Patedoye JC, Spyckerelle C. Quantitative characterization of internal defects in RDX crystals. Propell Explos Pyrot 1999;24(4):255–9.
[116] Cady HH. Growth and defects of explosives crystals. MRS OPL 1993;296:243–54.
[117] Yan T, Wang JH, Liu YC, Zhao J, Yuan JM, Guo JH. Growth and morphology of 1,3,5,7-tetranitro-1,3,5,7-tetraazacy-clooct ane (HMX) crystal. J Cryst Growth 2015;430(1125):7–13.
[118] Chapman HN, Nugent KA. Coherent lensless X-ray imaging. Nat Photonics 2010;4(12):833–9.
[119] Yau A, Cha W, Kanan MW, Stephenson GB, Ulvestad A. Bragg coherent diffractive imaging of single-grain defect dynamics in polycrystalline films. Science 2017;356(6339):739–42.
[120] Williams GJ, Pfeifer MA, Vartanyants IA, Robinson IK. Three-dimensional imaging of microstructure in Au nanocrystals. Phys Rev Lett 2003;90(17):175501.
[121] Barty A, Marchesini S, Chapman HN, Cui C, Howells MR, Shapiro DA, et al. Three-dimensional coherent X-ray diffraction imaging of a ceramic nanofoam: determination of structural deformation mechanisms. Phys Rev Lett 2008;101(5):055501.
[122] Kawaguchi T, Keller TF, Runge H, Gelisio L, Seitz C, Kim YY, et al. Gas–induced segregation in Pt-Rh alloy nanoparticles observed by *in situ* Bragg coherent diffraction imaging. Phys Rev Lett 2019;123(24):246001.
[123] Robinson IK, Vartanyants IA, Williams GJ, Pfeifer MA, Pitney JA. Reconstruction of the shapes of gold nanocrystals using coherent X-ray diffraction. Phys Rev Lett 2001;87(19):195505.
[124] Giewekemeyer K, Thibault P, Kalbfleisch S, Beerlink A, Kewish CM, Dierolf M, et al. Quantitative biological imaging by ptychographic X-ray diffraction microscopy. Proc Natl Acad Sci USA 2010;107(2):529–34.
[125] Barty A, Boutet S, Bogan MJ, Hau-Riege S, Marchesini S, Sokolowski-Tinten K, et al. Ultrafast single-shot diffraction imaging of nanoscale dynamics. Nat Photonics 2008;2(7):415–9.
[126] Robinson I, Harder R. Coherent X-ray diffraction imaging of strain at the nanoscale. Nat Mater 2009;8(4):291–8.
[127] Favre-Nicolin V, Mastropietro F, Eymery J, Camacho D, Niquet Y, Borg B, et al. Analysis of strain and stacking faults in single nanowires using Bragg coherent diffraction imaging. New J Phys 2010;12(3):035013.
[128] Cherukara MJ, Pokharel R, O'Leary TS, Baldwin JK, Maxey E, Cha W, et al. Three-dimensional X-ray diffraction imaging of dislocations in polycrystalline metals under tensile loading. Nat Commun 2018;9(1):1–6.
[129] Ziaja B, Chapman H, Fäustlin R, Hau-Riege S, Jurek Z, Martin A, et al. Limitations of coherent diffractive imaging of single objects due to their damage by intense X-ray radiation. New J Phys 2012;14(11):115015.
[130] Fan J, Sun Z, Wang Y, Park J, Kim S, Gallagher-Jones M, et al. Single-pulse enhanced coherent diffraction imaging of bacteria with an X-ray free-electron laser. Sci Rep 2016;6(1):34008.
[131] Rath AD, Timneanu N, Maia FR, Bielecki J, Fleckenstein H, Iwan B, et al. Explosion dynamics of sucrose nanospheres monitored by time of flight spectrometry and coherent diffractive imaging at the split-and-delay beam line of the FLASH soft X-ray laser. Opt Express 2014;22(23):28914–25.
[132] Ravindran S, Tessema A, Kidane A. Multiscale damage evolution in polymer bonded sugar under dynamic loading. Mech Mater 2017;114:97–106.
[133] Spitzer D, Risse B, Schnell F, Pichot V, Klaumünzer M, Schaefer MR. Continuous engineering of nano-cocrystals for medical and energetic applications. Sci Rep 2014;4(1):6575.
[134] Rossi C, Zhang K, Esteve D, Alphonse P, Tailhades P, Vahlas C. Nanoenergetic materials for MEMS: a review. J Microelectromech Syst 2007;16(4):919–31.
[135] Sundaram D, Yang V, Yetter RA. Metal-based nanoenergetic materials: synthesis, properties, and applications. Prog Energ Combust 2017;61:293–365.
[136] Chen S, Chai HW, He AM, Tschentscher T, Cai Y, Luo SN. Resolving dynamic fragmentation of liquids at the nanoscale with ultrafast small-angle X-ray scattering. J Synchrotron Radiat 2019;26(Pt 5):1412–21.
[137] Zhang TF, Ma Z, Li GP, Wang Z, Zhao BB, Luo YJ. Electrostatic interactions for directed assembly of high performance nanostructured energetic materials of Al/Fe_2O_3/multiwalled carbon nanotube (MWCNT). J Solid State Chem 2016;237:394–403.
[138] Tang DY, Lyu J, He W, Chen J, Yang G, Liu PJ, et al. Metastable intermixed core-shell Al@M$(IO_3)_x$ nanocomposites with improved combustion efficiency by using tannic acid as a functional interfacial layer. Chem Eng J 2020;384:123369.
[139] Zhou X, Wang YJ, Cheng ZP, Ke X, Jiang W. Facile preparation and energetic characteristics of core–shell Al/CuO metastable intermolecular composite thin film on a silicon substrate. Chem Eng J 2017;328:585–90.
[140] Liu HC, Zhang JD, Gou JY, Sun YY. Preparation of Fe_2O_3/Al composite powders by homogeneous precipitation method. Adv Powder Technol 2017;28(12):3241–6.
[141] Bellitto VJ, Melnik MI, Sherlock MH, Chang JC, O'Connor JH, Mackey JA. Microstructure effects on the detonation velocity of a heterogeneous high-explosive. J Energ Mater 2018;36(4):485–92.
[142] Horie Y. Hot spots, high explosives ignition, and material microstructure. Mater Sci Forum 2014;767:3–12.
[143] Maienschein J. Research topics in explosives—a look at explosives behaviors. J Phys Conf Ser 2014;500:052027.
[144] Wang H, Xu J, Sun S, Liu Y, Zhu C, Li J, et al. Characterization of crystal microstructure based on small angle X-ray scattering (SAXS) technique. Molecules 2020;25(3):443.
[145] Viecelli J, Ree F. Carbon clustering kinetics in detonation wave propagation. J Appl Phys 1999;86(1):237–48.
[146] Bastea S. Aggregation kinetics of detonation nanocarbon. Appl Phys Lett 2012;100(21):214106.
[147] Bastea S. Nanocarbon condensation in detonation. Sci Rep 2017;7(1):42151.
[148] Mang J, Skidmore C, Howe P, Hjelm R, Rieker T. Structural characterization of energetic materials by small angle scattering. AIP Conf Proc 2000;505:699–702.
[149] Willey TM, Van Buuren T, Lee JR, Overturf GE, Kinney JH, Handly J, et al. Changes in pore size distribution upon thermal cycling of TATB-based explosives measured by ultra-small angle X-ray scattering. Propell Explos Pyrot 2006;31(6):466–71.
[150] Capatina D, D'Amico K, Nudell J, Collins J, Schmidt O. DCS—a high flux beamline for time resolved dynamic compression science—design highlights. AIP Conf Proc 2016;1741:030036.
[151] Bagge-Hansen M, Lauderbach L, Hodgin R, Bastea S, Fried L, Jones A, et al. Measurement of carbon condensates using small-angle X-ray scattering during detonation of the high explosive hexanitrostilbene. J Appl Phys 2015;117(24):245902.
[152] Gustavsen RL, Dattelbaum DM, Watkins EB, Firestone MA, Podlesak DW, Jensen BJ, et al. Time resolved small angle X-ray scattering experiments performed on detonating explosives at the advanced photon source: Calculation of the time and distance between the detonation front and the X-ray beam. J Appl Phys 2017;121(10):105902.
[153] Huber RC, Ringstrand BS, Dattelbaum DM, Gustavsen RL, Seifert S, Firestone MA, et al. Extreme condition nanocarbon formation under air and argon atmospheres during detonation of composition B-3. Carbon 2018;126:289–98.
[154] Chen S, Luo SN. Small-angle scattering of polychromatic X-rays: effects of bandwidth, spectral shape and high harmonics. J Synchrotron Radiat 2018;25(Pt 2):496–504.
[155] Hammons JA, Nielsen MH, Bagge-Hansen M, Bastea S, Shaw WL, Lee JR, et al. Resolving detonation nanodiamond size evolution and morphology at sub-microsecond timescales during high-explosive detonations. J Phys Chem C 2019;123(31):19153–64.
[156] Hammons JA, Nielsen MH, Bagge-Hansen M, Lauderbach LM, Hodgin RL, Bastea S, et al. Observation of variations in condensed carbon morphology dependent on composition B detonation conditions. Propell Explos Pyrot 2020;45(2):347–55.
[157] Dreizin EL. Metal-based reactive nanomaterials. Prog Energ Combust 2009;35(2):141–67.
[158] He W, Liu PJ, He GQ, Gozin M, Yan QL. Highly reactive metastable intermixed composites (MICs): preparation and characterization. Adv Mater 2018;30(41):e1706293.
[159] Jacob RJ, Jian G, Guerieri PM, Zachariah MR. Energy release pathways in nanothermites follow through the condensed state. Combust Flame 2015;162(1):258–64.
[160] Shende R, Subramanian S, Hasan S, Apperson S, Thiruvengadathan R, Gangopadhyay K, et al. Nanoenergetic composites of CuO nanorods, nanowires, and Al-nanoparticles. Propell Explos Pyrot 2008;33(2):122–30.
[161] Walker JD, Tannenbaum R. Characterization of the sol-gel formation of iron (III) oxide/hydroxide nanonetworks from weak base molecules. Chem Mater 2006;18(20):4793–801.

[162] Son SF. Performance and characterization of nanoenergetic materials at Los Alamos. Mater Res Soc 2003;800(AA5):2.
[163] Qin L, Gong T, Hao H, Wang K, Feng H. Core–shell structured nanothermites synthesized by atomic layer deposition. J Nanopart Res 2013;15(12):2150.
[164] Wang J, Qiao Z, Yang Y, Shen J, Long Z, Li Z, et al. Core–shell Al–polytetrauoroethylene (PTFE) configurations to enhance reaction kinetics and energy performance for nanoenergetic materials. Chemistry 2016;22(1):279–84.
[165] Chen S, E J, Luo SN. SLADS: a parallel code for direct simulations of scattering of large anisotropic dense nanoparticle systems. J Appl Cryst 2017;50(3):951–8.
[166] Lu L, Bie BX, Li QH, Sun T, Fezzaa K, Gong XL, et al. Multiscale measurements on temperature-dependent deformation of a textured magnesium alloy with synchrotron X-ray imaging and diffraction. Acta Mater 2017;132:389–94.
[167] Zhao YL, Li GG, Hou HM, Shi JC, Luo SN. CN and C_2 formation mechanisms in fs-laser induced breakdown of nitromethane in Ar or N_2 atmosphere. J Hazard Mater 2020;393:122396.
[168] Campbell MB, Heilweil EJ. Noninvasive detection of weapons of mass destruction using terahertz radiation. Proc SPIE 2003;5070:38–43.
[169] Guo L, Hu Y, Zhang Y, Zhang C, Chen Y, Zhang XC. Vibrational spectrum of γ-HNIW investigated using terahertz time-domain spectroscopy. Opt Express 2006;14(8):3654–9.
[170] Melinger JS, Laman N, Grischkowsky D. The underlying terahertz vibrational spectrum of explosives solids. Appl Phys Lett 2008;93(1):011102.
[171] Melinger JS, Harsha SS, Laman N, Grischkowsky D. Temperature dependent characterization of terahertz vibrations of explosives and related threat materials. Opt Express 2010;18(26):27238–50.
[172] Damarla G, Venkatesh M, Chaudhary AK. Temperature-dependent terahertz spectroscopy and refractive index measurements of aqua-soluble and plastic explosives. Appl Opt 2018;57(29):8743–50.
[173] Zhang W, Nickel D, Mittleman D. High-pressure cell for terahertz time-domain spectroscopy. Opt Express 2017;25(3):2983–93.
[174] Lewis W. Nevada test site-directed research and development, FY 2007 Report. Technical Report. Oak Ridge: US Department of Energy; 2006. Report No.: DOE/NV/25946-022; DOE/NV/11718-1245. Contract No.: DE-AC52-06NA25946.
[175] Gebs R, Klatt G, Janke C, Dekorsy T, Bartels A. High-speed asynchronous optical sampling with sub-50 fs time resolution. Opt Express 2010;18(6):5974–83.
[176] Brown KE, McGrane SD, Bolme CA, Moore DS. Ultrafast chemical reactions in shocked nitromethane probed with dynamic ellipsometry and transient absorption spectroscopy. J Phys Chem A 2014;118(14):2559–67.
[177] Bowlan P, Powell M, Perriot R, Martinez E, Kober EM, Cawkwell MJ, et al. Probing ultrafast shock-induced chemistry in liquids using broad-band mid-infrared absorption spectroscopy. J Chem Phys 2019;150(20):204503.
[178] Holmes NC, Nellis WJ, Graham WB, Walrafen GE. Spontaneous Raman scattering from shocked water. Phys Rev Lett 1985;55(22):2433–6.
[179] Schmidt S, Moore D, Shaner J, Shampine D, Holt W. Coherent anti-stokes Raman scattering in benzene and nitromethane shock-compressed to 10 GPa. Physica 1986;139:587–9.
[180] Tas G, Franken J, Hambir SA, Hare DE, Dlott DD. Ultrafast Raman spectroscopy of shock fronts in molecular solids. Phys Rev Lett 1997;78(24):4585–8.
[181] Miller JE, Boehly TR, Melchior A, Meyerhofer DD, Celliers PM, Eggert JH, et al. Streaked optical pyrometer system for laser-driven shock-wave experiments on OMEGA. Rev Sci Instrum 2007;78(3):034903.
[182] Zhang C, Liu H, Duan X, Liu Y, Zhang H, Sun L, et al. Study of M-band X-ray preheating effect on shock propagation via streaked optical pyrometer system at SG-III prototype lasers. Phys Plasmas 2019;26(1):012708.
[183] Bouyer V, Darbord I, Hervé P, Baudin G, Le Gallic C, Clément F, et al. Shock-to-detonation transition of nitromethane: time-resolved emission spectroscopy measurements. Combust Flame 2006;144(1–2):139–50.
[184] Shaik AK, Epuru NR, Syed H, Byram C, Soma VR. Femtosecond laser induced breakdown spectroscopy based standoff detection of explosives and discrimination using principal component analysis. Opt Express 2018;26(7):8069–83.
[185] Rao EN, Sunku S, Rao SV. Femtosecond laser-induced breakdown spectroscopy studies of nitropyrazoles: the effect of varying nitro groups. Appl Spectrosc 2015;69(11):1342–54.
[186] Gottfried JL, De Lucia FC Jr, Munson CA, Miziolek AW. Double-pulse standoff laser-induced breakdown spectroscopy for versatile hazardous materials detection. Spectrochim Acta B At Spectrosc 2007;62(12):1405–11.
[187] Dikmelik Y, McEnnis C, Spicer JB. Femtosecond and nanosecond laser-induced breakdown spectroscopy of trinitrotoluene. Opt Express 2008;16(8):5332–7.
[188] Dong M, Lu J, Yao S, Zhong Z, Li J, Li J, et al. Experimental study on the characteristics of molecular emission spectroscopy for the analysis of solid materials containing C and N. Opt Express 2011;19(18):17021–9.
[189] Ran PX, Hou HM, Luo SN. Molecule formation induced by non-uniform plume–air interactions in laser induced plasma. J Anal At Spectrom 2017;32(11):2254–62.
[190] Civiš M, Civiš S, Sovová K, Dryahina K, Španěl P, Kyncl M. Laser ablation of FOX-7: proposed mechanism of decomposition. Anal Chem 2011;83(3):1069–77.
[191] Hori T, Akamatsu F. Laser-induced breakdown plasma observed using a streak camera. Jpn J Appl Phys 2008;47(6R):4759–61.
[192] Rabasovic MS, Rabasovic MD, Marinkovic BP, Sevic D. Laser-induced plasma measurements using Nd: YAG laser and streak camera: Timing considerations. Atoms 2019;7(1):6.
[193] Celliers PM, Bradley DK, Collins GW, Hicks DG, Boehly TR, Armstrong WJ. Line-imaging velocimeter for shock diagnostics at the OMEGA laser facility. Rev Sci Instrum 2004;75(11):4916–29.
[194] Celliers PM, Erskine DJ, Sorce CM, Braun DG, Landen OL, Collins GW. A high-resolution two-dimensional imaging velocimeter. Rev Sci Instrum 2010;81(3):035101.
[195] Greenfield SR, Casson JL, Koskelo AC. Nanosecond interferometric studies of surface deformations of dielectrics induced by laser irradiation. In: Proceedings of the Laser-Induced Damage in Optical Materials: 1999; 1999 Oct 4–7; Boulder, CO, USA; 2000.
[196] Gahagan KT, Moore DS, Funk DJ, Reho JH, Rabie RL. Ultrafast interferometric microscopy for laser-driven shock wave characterization. J Appl Phys 2002;92(7):3679–82.
[197] Temnov VV, Sokolowski-Tinten K, Von der Zhou P, Linde D. Femtosecond time-resolved interferometric microscopy. Appl Phys A Mater Sci Process 2004;78(4):483–9.
[198] Greenfield SR, Luo SN, Paisley DL, Loomis EN, Swift DC, Koskelo AC. Transient imaging displacement interferometry applied to shock loading. AIP Conf Proc 2007;955(1):1093–6.
[199] Wu Y, Wang F, Wang Q, Li Y, Jiang S. A high temporal resolution numerical algorithm for shock wave velocity diagnosis. Sci Rep 2019;9(1):8597.